

H I CLOUDS IN THE LOWER HALO: I. THE GALACTIC ALL-SKY SURVEY PILOT REGION

H. ALYSON FORD^{1,2}, N. M. MCCLURE-GRIFFITHS², FELIX J. LOCKMAN³, J. BAILIN⁴, M. R. CALABRETTA², P. M. W. KALBERLA⁵, T. MURPHY^{6,7}, D. J. PISANO³

Accepted for publication in ApJ

ABSTRACT

We have detected over 400 H I clouds in the lower halo of the Galaxy within the pilot region of the Galactic All-Sky Survey (GASS), a region of the fourth quadrant that spans 18° in longitude, 40° in latitude and is centered on the Galactic equator. These clouds have a median peak brightness temperature of 0.6 K, a median velocity width of 12.8 km s^{-1} , and angular sizes $\lesssim 1^\circ$. The motion of these clouds is dominated by Galactic rotation with a random cloud-to-cloud velocity dispersion of 18 km s^{-1} . A sample of clouds likely to be near tangent points was analyzed in detail. These clouds have radii on the order of 30 pc and a median H I mass of $630 M_\odot$. The population has a vertical scale height of 400 pc and is concentrated in Galactocentric radius, peaking at $R = 3.8 \text{ kpc}$. This confined structure suggests that the clouds are linked to spiral features, while morphological evidence that many clouds are aligned with loops and filaments is suggestive of a relationship with star formation. The clouds might result from supernovae and stellar winds in the form of fragmenting shells and gas that has been pushed into the halo rather than from a galactic fountain.

Subject headings: galaxies: structure — Galaxy: halo — ISM: clouds — ISM: structure — radio lines: ISM

1. INTRODUCTION

Neutral atomic hydrogen (H I) is ubiquitous throughout the Galaxy with a wide variety of morphologies and kinematics, and exhibits many complex structures, including worms (Koo et al. 1992), sheets and filaments (Heiles 1967; Dickey & Lockman 1990), shells (Heiles 1979; McClure-Griffiths et al. 2002), and clouds (Lockman 2002). The Galactic H I disk extends to Galactocentric radii, $R \geq 30 \text{ kpc}$ and its thickness varies from $\leq 100 \text{ pc}$ inside $R = 3.5 \text{ kpc}$ to $\sim 3 \text{ kpc}$ in the outer Galaxy, with a roughly uniform thickness of 230 pc between 3.5 kpc and the solar circle (see Ferrière 2001 and references within). H I is also known to extend far beyond the thin H I disk as a layer into the Galactic halo (Lockman 1984). However, recent high angular resolution observations using the Green Bank Telescope (GBT) have revealed that this layer is not smooth but instead is composed of small H I clouds with sizes on the order of a few tens of parsecs and masses of $50 M_\odot$ (Lockman 2002); confusion may limit the detectability of such clouds at low heights, in which case they may not be confined to the halo (see, e.g., Stil et al. 2006). These clouds follow Galactic rotation and are discrete clumps of H I that are localized in space and velocity. Although they are sometimes related to larger structures, for example, em-

bedded in filaments, each cloud appears to be a distinct object. The gross properties of the Milky Way's thick H I layer may in fact be a consequence of the statistical properties of these H I clouds and it is possible that thick H I disks in other galaxies, once observed with sufficient resolution, would reveal a similar structure.

While the origin of the halo clouds is unknown, one possible explanation is a “galactic fountain” model, where hot gas produced by supernovae rises into the halo of the Galaxy, cools and condenses into H I clouds, which then fall back to the plane (Shapiro & Field 1976; Bregman 1980). Houck & Bregman (1990) predicted that, from a lower temperature fountain, gas in Galactic rotation could be formed at heights close to the plane. This scenario is supported by observations of intermediate velocity clouds (IVCs), such as those of cloud g1, whose location, kinematics and abundances match those expected (Wakker et al. 2008). The abundances in the IV Arch (Richter et al. 2001b) and LLIV Arch (Richter et al. 2001a) also suggest a fountain origin; as their abundances are near solar it is likely that they originated from material enriched from the disk. The location of these IVCs also support this, as they are roughly 1 kpc from the disk.

Another possibility is that the halo clouds originate in environments where supernovae and stellar winds disrupt the surrounding medium. Such events can result in the formation of a bubble, and models suggest that with a large enough energy source it is possible for these bubbles to expand beyond the thickness of the Galactic disk (e.g., Tomisaka & Ikeuchi 1988; Heiles 1990). These bubbles are encompassed by an H I shell as a result of either radiative cooling, which then accumulates more H I as the bubble continues to expand, or solely the sweeping up of ambient material, depending on the wind speed (Koo & McKee 1992). The shell remains as a single entity until in some cases Rayleigh-Taylor instabilities cause it to fragment (Mac Low et al. 1989). Once

¹ Center for Astrophysics and Supercomputing, Swinburne University of Technology, Mail H39, P.O. Box 218, Hawthorn, Victoria 3122, Australia; alyson@astro.swin.edu.au

² Australia Telescope National Facility, CSIRO, P.O. Box 76, Epping, NSW 1710, Australia.

³ National Radio Astronomy Observatory, P.O. Box 2, Green Bank, WV 24944, USA.

⁴ Department of Physics & Astronomy, McMaster University, 1280 Main Street West, Hamilton, ON, L8S 4M1, Canada.

⁵ Radioastronomisches Institut der Universität Bonn, Auf dem Hügel 71, 53121 Bonn, Germany.

⁶ School of Physics, University of Sydney, NSW 2006, Australia.

⁷ School of Information Technologies, University of Sydney, NSW 2006, Australia.

this fragmentation has occurred, gas that has been shock heated is expelled outwards, mixing material from the disk with that in the halo (Norman & Ikeuchi 1989) and the remaining fragments of the H I shell may be the observed halo clouds (McClure-Griffiths et al. 2006). It is also possible for the hot gas that has been expelled to cool and recombine, as seen in models of de Avillez (2000), or perhaps energy from increased supernova activity in areas of active star formation has simply pushed disk gas into the halo, forming clumps of H I.

Large samples of halo clouds are required to constrain the properties and distribution of the population and provide insight into their origin. As the Lockman (2002) sample only has 38 clouds in a small region of the Galaxy, the properties of the population that constitute the H I layer are currently not well-determined. In this paper we present a catalog of over 400 H I clouds in the lower halo of the inner Galaxy, which we have detected in the Galactic All-Sky Survey pilot region, along with an analysis and discussion of their properties and distribution. We begin with an overview of the observations and data in §2 and present the observed properties of all clouds in §3. In §4 we determine the physical properties of a subset of these clouds that can be assumed to be located at tangent points, where the observer’s line-of-sight is tangent to circles of constant Galactocentric radius. An analysis of the cloud properties is presented in §5 and implications of these results are discussed in §6. We summarize the results and discuss future work in §7.

2. OBSERVATIONS AND DATA

The data presented in this paper are from the Galactic All-Sky Survey (GASS), a fully sampled Galactic H I survey that covers the entire sky south of declination $\delta = 0^\circ$. GASS data were taken with the 21 cm Multibeam receiver (Staveley-Smith et al. 1996) at the Parkes Radio Telescope and cover $-400 \leq V_{\text{LSR}} \leq 450 \text{ km s}^{-1}$, where V_{LSR} is the velocity with respect to the local standard of rest. The spectral resolution of the data is 0.8 km s^{-1} and the half power beam width of the Multibeam is $\sim 15'$.

GASS observations began in 2005 January and were completed by the end of 2006. Data reduction was performed using the Livedata package, which is part of the ATNF subset of the aips++ distribution. The bandpass correction was performed using an algorithm designed specifically for GASS data and the Doppler correction was applied. Fluxes were calibrated from observations of the standards S6, S8 and S9 (Williams 1973). The reduced data were gridded into a 3D data cube with voxel dimensions of $4' \times 4' \times 0.8 \text{ km s}^{-1}$ using the Gridzilla package, which is also part of the ATNF subset of the aips++ distribution, and was based on the gridding algorithm described in Barnes et al. (2001). The rms spectral noise, $\Delta T_b \sim 60 \text{ mK}$, was determined by measuring brightness temperature fluctuations in a ~ 200 square degree region of the survey that spanned 48 velocity channels free of any obvious emission. The final GASS data release will be corrected for stray radiation according to the procedure described in Kalberla et al. (2005). Further details on GASS can be found in McClure-Griffiths et al. (2006), while extensive details will be presented in a future paper.

In this paper we present results from the GASS pilot region, a region that was chosen for a preliminary study

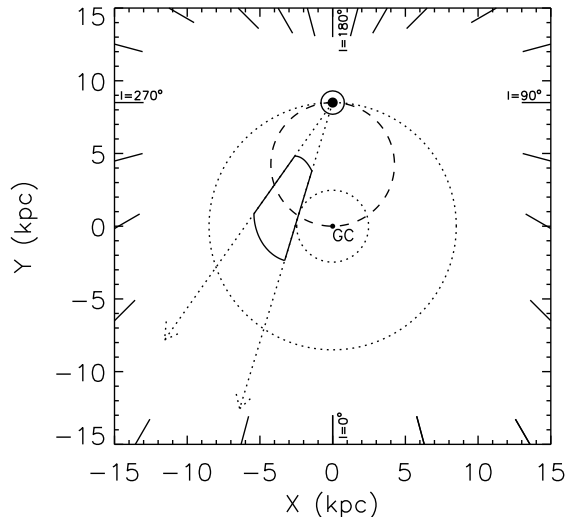


FIG. 1.— The area of the Galaxy discussed in this paper is bound by the longitude limits of the GASS pilot region (dotted arrows) and by $V_{\text{LSR}} = -70 \text{ km s}^{-1}$, which, for a flat rotation curve, gives the area enclosed by the solid line. Dotted circles mark Galactocentric radii of 2.47 kpc and 8.5 kpc and the locus of tangent points is shown by the dashed curve that connects the Sun and the Galactic center.

on halo clouds to develop techniques that will be applied to the entire survey in the future. The GASS pilot region is in the fourth quadrant in the inner Galaxy and spans $325^\circ \lesssim l \lesssim 343^\circ$, $|b| \lesssim 20^\circ$, and $-200 \leq V_{\text{LSR}} \leq -70 \text{ km s}^{-1}$ (see Figure 1). Our focus is on spatially discrete H I features with an angular size $\lesssim 1^\circ$. These features are not characteristic of stray radiation, so although these data have not been corrected for stray radiation, it is unlikely that any of the clouds discussed here are a spurious result of this effect.

3. HI CLOUDS IN THE GASS PILOT REGION

We detect numerous discrete H I features in the lower halo of the Galaxy with angular sizes $\lesssim 1^\circ$, similar to the population of halo clouds discovered by Lockman (2002). Samples of these clouds can be seen in Figures 2 and 3, where we display a longitude-latitude image at $V_{\text{LSR}} = -105 \text{ km s}^{-1}$ and a latitude-velocity image at $l = 334.60^\circ$, respectively. The curved lines at the top and bottom of Figure 2 represent the boundaries of the region studied in this paper. The contour in Figure 3 represents $T_b = 3 \text{ K}$. Where the emission is brighter than this it is difficult to distinguish clouds because of confusion, although we do detect some clouds above this threshold. These figures clearly demonstrate the presence of discrete H I clouds at a variety of longitudes, latitudes and velocities, which are seen both close to the disk and into the halo. Some clouds are extended and some compact, and many appear to be related to diffuse and filamentary structures.

3.1. Search Method and Criteria

We chose the following selection criteria to generate a homogeneously selected catalog of halo clouds:

1. The cloud must be within the GASS pilot region, i.e., within $324.7^\circ \leq l \leq 343.1^\circ$, $|b| \lesssim 20^\circ$ (see Figure 2 for exact boundaries), and $-200 \leq V_{\text{LSR}} \leq -70 \text{ km s}^{-1}$.
2. The cloud must span four or more pixels and be clearly visible over three or more channels in the spectra.

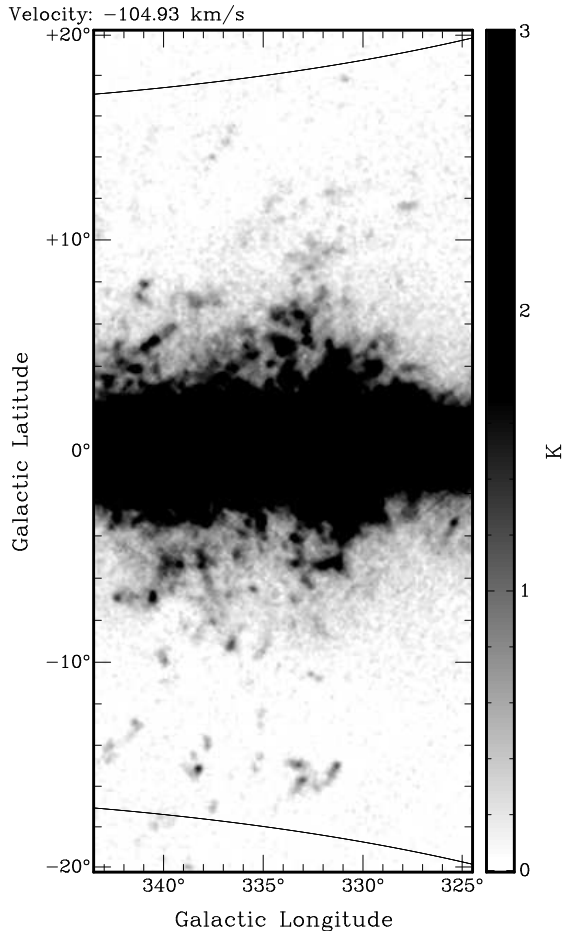


FIG. 2.— GASS pilot region at $V_{\text{LSR}} = -105 \text{ km s}^{-1}$. Many H I clouds with angular sizes $\lesssim 1^\circ$ are observed, both near the Galactic plane and into the lower halo. The curved lines at the top and bottom are the boundaries of the region searched.

Most cloud detections were made with $T_b \geq 5\Delta T_b$, where $\Delta T_b = 60 \text{ mK}$.

3. The cloud must be distinguishable from unrelated background emission. It was impossible to separate clouds from this emission at low latitudes in the least negative velocity channels, where the emission is particularly complex.

We believe that we have identified all obvious clouds that meet the criteria listed above. However, it should be noted that some clouds appeared to have double-peaked velocity profiles. In these circumstances, each peak was cataloged as an individual cloud because confusion may be important. If so, confusion may have resulted in the merging of profiles of multiple clouds at similar locations but with distinct velocities, resulting in a double-peaked profile. We will discuss such effects in detail in a subsequent publication.

Most of the clouds are not isolated and spherical, but are instead often part of nebulous, filamentary structures and/or sitting in a fluctuating diffuse background. As a result, all automated cloud finding algorithms that we tested had difficulty differentiating clouds from neighbouring clouds and from background emission. Clouds were therefore identified and their properties measured by visual inspection of the data cubes.

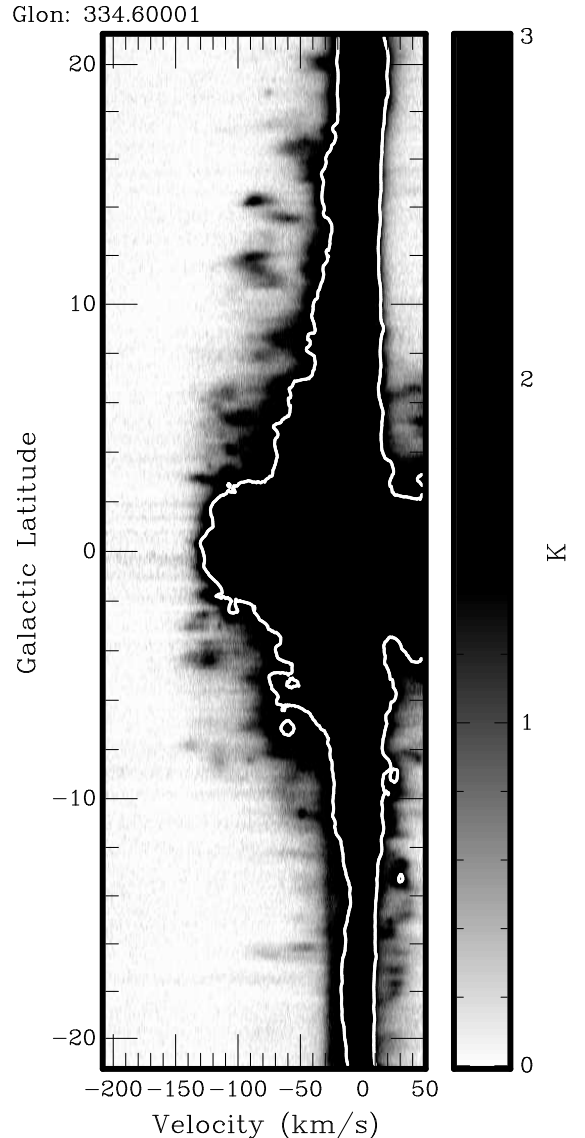


FIG. 3.— H I clouds are observed at a variety of velocities, as can be seen in this latitude–velocity diagram at $l = 334.60^\circ$. The contour represents $T_b = 3 \text{ K}$, which is the brightness temperature above which few clouds can be distinguished due to confusion.

3.2. Properties of the Entire Cloud Sample

Using the criteria presented in §3.1 we measured 403 H I clouds in the GASS pilot region. The observed properties of these clouds are presented in Table 1. We provide a description of each property and how it was determined below, along with sample spectra in Figure 4. An integrated intensity map, which has the summed intensities over the velocity range for a given cloud, was used to aid in the determination of some properties. These maps have had a background subtracted that was the mean flux of unrelated emission in three interactively chosen areas surrounding the cloud. It is apparent from Figure 5 that at the low end of the peak brightness temperature distribution ($\lesssim 0.5 \text{ K}$) there is significant incompleteness in regions of higher background levels. We are confident in our background subtraction because beyond incompleteness there is no trend between the peak brightness temperature and mean background level.

The columns in Table 1 are:

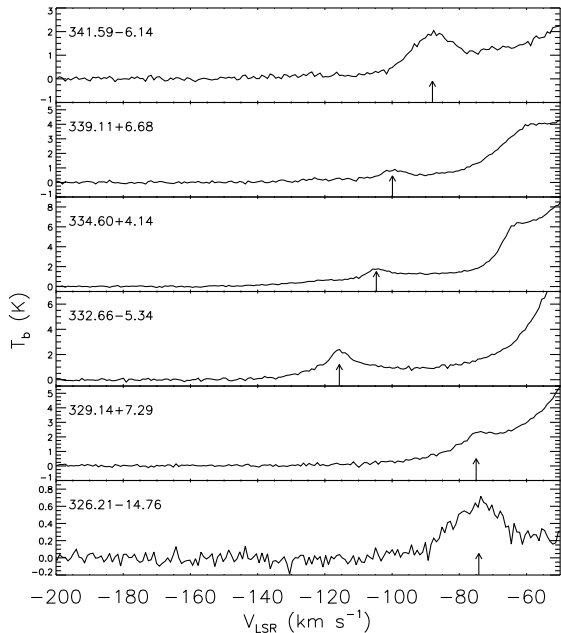


FIG. 4.— Spectra from a random sample of H I clouds from Table 1. Many clouds appear to be sitting on broad spectral wings. Arrows mark the velocity where the brightness temperature peaks (after background subtraction) for each profile.

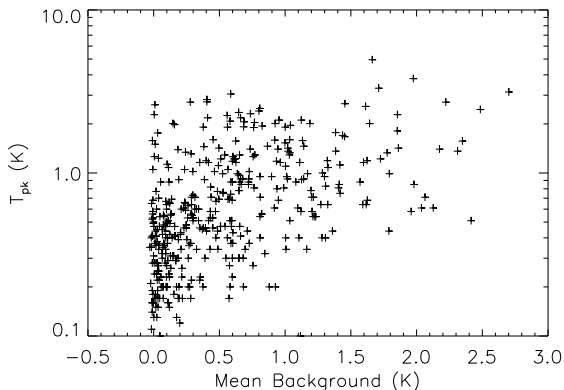


FIG. 5.— Peak brightness temperature as a function of the mean background subtracted from the integrated intensity map. In regions of high background levels there is a clear decline in the number of clouds with low peak brightness temperatures.

Columns 1-2: The Galactic longitude, l , and latitude, b , of the cloud at the position of the peak brightness temperature.

Column 3: The cloud velocity with respect to the local standard of rest, V_{LSR} , in km s^{-1} , measured as the velocity of the cloud’s peak brightness temperature after background subtraction. The background level was determined by fitting a line between each edge of the cloud velocity profile where it merges with surrounding emission.

Column 4: The cloud’s peak brightness temperature after background subtraction, T_{pk} , in K. Most clouds that we measured had $T_b < 3$ K prior to background subtraction, as clouds with T_b greater than this tended to be found only in areas of high confusion.

Column 5: Δv is the full-width at half-maximum (FWHM) of the velocity profile, determined by inspection after background subtraction, in km s^{-1} .

Column 6: The H I column density, N_{HI} , at the cloud center is $1.94 \times 10^{18} T_{\text{pk}} \Delta v \text{ cm}^{-2}$ in the optically thin limit, an assumption that is reasonable because the emission is faint. N_{HI} was determined after we subtracted a background from the integrated intensity map. The background level was highly variable from cloud to cloud being mainly dependent on the latitude and velocity of the cloud.

Column 7: θ_{maj} and θ_{min} are the maximum and minimum extent of the cloud in arcminutes and were determined by inspection from the integrated intensity map of the cloud. Many of the clouds are unresolved in at least one dimension but we have not deconvolved their angular sizes due to the uncertainties associated with the fluctuating background levels of the integrated intensity maps. These values therefore represent upper limits of the angular extent.

Column 8: $M_{\text{HI}} d^{-2}$ represents the H I mass of the cloud in units of $M_{\odot} \text{ kpc}^{-2}$, where d is the distance to the cloud in kpc. A background was subtracted from the integrated intensity map, thereby leaving only the flux of the cloud, which was then summed. The mass also relies on the assumption that the H I is optically thin.

Column 9: Details of prior detections in the literature, if any, are noted.

3.3. Uncertainties in Observed Properties

δV_{LSR} : The difference between V_{LSR} and the velocity where the profile decreases from the peak by $\sqrt{\Delta T_b^2 + \delta T_{\text{pk}}^2}$, assuming the profile can be approximated by a Gaussian, where δT_{pk} is the error on T_{pk} (see below) and ΔT_b is the rms noise.

δT_{pk} : This error is assumed to be $\sqrt{\Delta T_b^2 + (\Delta T_b / \sqrt{2})^2}$, where the first term represents the error in T_{pk} prior to the background subtraction and the second term represents the error of the mean of the two points defining the background.

$\delta \Delta v$: Each of the two half maximum points on the profile is defined as the point where the profile, with error ΔT_b , crosses $(1/2)T_{\text{pk}}$, with error $(1/2)\delta T_{\text{pk}}$. We translate these T_b errors into velocity errors using the slope of a Gaussian profile. We also add the channel width in quadrature.

δN_{HI} : The error on the H I column density, $\delta N_{\text{HI}} = N_{\text{HI}} \sqrt{(\delta T_{\text{pk}} / T_{\text{pk}})^2 + (\delta \Delta v / \Delta v)^2}$.

$\delta \theta_{\text{maj}}$ and $\delta \theta_{\text{min}}$: The uncertainties due to the interactive nature of the angular extent measurements and the fluctuating background levels of the integrated intensity maps dominate over the nominal statistical error. The uncertainties were therefore calibrated by comparing values obtained during different trials for a randomly selected subset of clouds and are estimated to be approximately 25% of the determined angular extent.

$\delta M_{\text{HI}} d^{-2}$: The errors introduced by the interactive process of determining the cloud area and subtracting the background dominate the mass uncertainties and are estimated to be 40% of the determined mass, based on the comparison of different trials of randomly selected clouds mentioned above.

3.4. Observed Properties

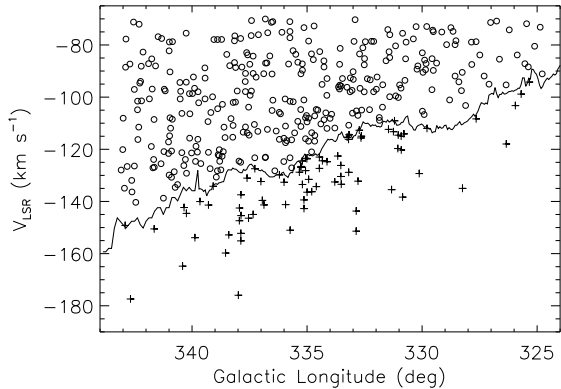


FIG. 6.— V_{LSR} as a function of longitude for all clouds in Table 1. Crosses represent a subset of clouds with $V_{\text{dev}} \leq 0.8 \text{ km s}^{-1}$ (the tangent point sample; §4) while circles represent all other GASS pilot region clouds. The solid line is the V_t curve determined by McClure-Griffiths & Dickey (2007) from H I observations for $l \leq 339.695^\circ$ and by Luna et al. (2006) from CO observations for all remaining longitudes. As we have searched for all clouds within $-200 < V_{\text{LSR}} \leq -70 \text{ km s}^{-1}$, the decline in the number of clouds at velocities more negative than the terminal velocity demonstrates that the kinematics of the clouds are dominated by Galactic rotation.

The V_{LSR} as a function of longitude for all clouds is shown in Figure 6, along with a solid line denoting the terminal velocity, V_t , which, in the fourth quadrant, is the most negative velocity permitted by Galactic rotation. The clouds are abundant at velocities allowed by Galactic rotation and there is clearly a decline in the number of clouds beyond (more negative than) V_t , which demonstrates that the motions of this cloud population are dominated by Galactic rotation. Clouds beyond V_t are said to have “forbidden velocities” and the amount their V_{LSR} differs from V_t is the deviation velocity, $V_{\text{dev}} = V_{\text{LSR}} - V_t$, as defined by Wakker (1991). For $l \leq 339.695$, we used V_t determined by McClure-Griffiths & Dickey (2007) from H I observations from the Southern Galactic Plane Survey (McClure-Griffiths et al. 2005). For all remaining longitudes we used V_t determined by Luna et al. (2006) from the Columbia-Universidad de Chile CO surveys.

In Figure 7 we display the latitude distribution with deviation velocity. For clouds beyond the terminal velocity (with negative deviation velocities), those at lower latitudes have larger absolute deviation velocities. This is likely an artefact, as the number of clouds would naturally fall off with both more negative deviation velocities and larger latitudes if they were dominated by Galactic rotation. There are, however, some outliers at large positive latitudes with very negative deviation velocities.

Histograms of T_{pk} , Δv and angular size are presented in Figures 8a–c, respectively. The majority of clouds have $T_{\text{pk}} \leq 1 \text{ K}$, with the median $T_{\text{pk}} = 0.6 \text{ K}$. The number of clouds decreases sharply below $T_{\text{pk}} \simeq 5\Delta T_b$ and suggests that the sample is sensitivity limited. The median FWHM of the velocity profiles is 12.8 km s^{-1} and very few clouds have linewidths larger than 30 km s^{-1} (Figure 8b). All but one of the linewidths are greater than 3.4 km s^{-1} ; as the velocity resolution of the survey is 0.8 km s^{-1} , most lines are therefore well resolved. The median angular diameter of the clouds is $29'$, which is approximately twice the beam size. This value and the steep cutoff at small angular sizes seen in Figure 8c are

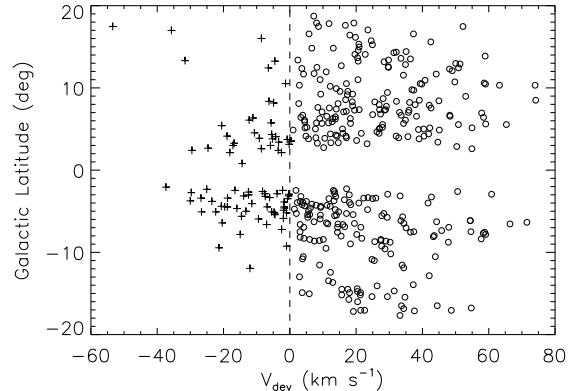


FIG. 7.— Latitude distribution with deviation velocity, V_{dev} , for all clouds in Table 1, where $V_{\text{dev}} = V_{\text{LSR}} - V_t$, as defined by Wakker (1991). We used V_t determined by McClure-Griffiths & Dickey (2007) from H I observations for $l \leq 339.695^\circ$ and by Luna et al. (2006) from CO observations for all remaining longitudes. Crosses denote a subset of clouds with $V_{\text{dev}} \leq 0.8 \text{ km s}^{-1}$ (the tangent point sample, §4), while circles denote all other clouds in the GASS pilot region. For clouds that are observed at forbidden velocities ($V_{\text{dev}} < 0 \text{ km s}^{-1}$, denoted by the dashed line), those further from the plane have smaller absolute deviation velocities. This trend is expected of a population of clouds whose kinematics are dominated by Galactic rotation, as the number of clouds would fall off at more negative velocities and larger latitudes, but there are some outliers at large positive latitudes with more negative deviation velocities.

most likely due to the spatial resolution limit of the data and suggest that many of the clouds are unresolved.

4. SELECTION OF A SET OF “TANGENT POINT” CLOUDS

The largest magnitude velocity from Galactic rotation in the inner Galaxy occurs at the tangent point, defined as the location where the line-of-sight is perpendicular to a circle of constant Galactocentric radius (see Figure 1). Here $R_t = R_0 |\sin l|$ and the LSR velocity from Galactic rotation is $V_t = R_0 [\Theta/R_t - \Theta_0/R_0] \sin l \cos b$, where R_0 is the radius of the solar circle, Θ is the circular velocity and Θ_0 is the circular velocity at the solar circle. We adopt $R_0 \equiv 8.5 \text{ kpc}$ and $\Theta_0 \equiv 220 \text{ km s}^{-1}$, as recommended by the IAU (Kerr & Lynden-Bell 1986). Clouds in pure Galactic rotation cannot have a circular velocity beyond V_t . However, the random motion of a cloud near the tangent point might increase the cloud’s $|V_{\text{LSR}}|$ beyond $|V_t|$. Clouds in Galactic rotation with $|V_{\text{LSR}}| \geq |V_t|$ must therefore lie near the tangent point and thus at a known distance, $d_t = R_0 \cos l / \cos b$. While an assumption, it is reasonable to adopt a distance of d_t for clouds with $|V_{\text{LSR}}| \geq |V_t|$ given the rapid decline in the number of clouds beyond the terminal velocity, as shown in Figure 6. Tangent point clouds constitute a sample uniquely suited for investigating the population’s distribution and properties, such as physical size and mass.

From the population of clouds detected in the GASS pilot region, we define the tangent point sample as all clouds with $V_{\text{LSR}} \leq V_t + 0.8 \text{ km s}^{-1}$, where 0.8 km s^{-1} is one channel width, and assume that they are at the tangent point; we assess the effect of this assumption in §5.3. We also assume that Galactic rotation is constant with distance from the plane, i.e., $\Theta(z) = \Theta(0)$; deviations from cylindrical rotation will be discussed in a subsequent work. As the tangent point clouds in the GASS pilot region are nearly all at the same distance and the latitude boundary of the region corresponds to a constant height of 2.5 kpc (at tangent points), they

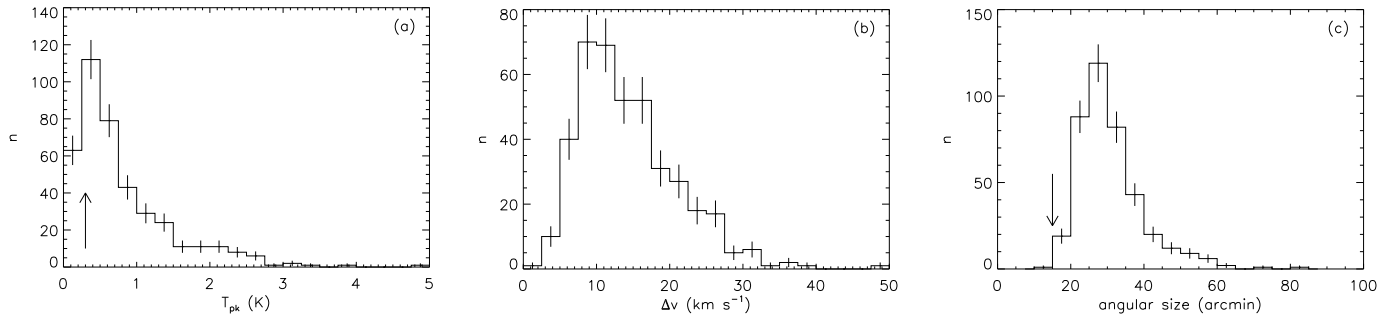


FIG. 8.— (a) Histogram of the peak brightness temperature of the clouds, T_{pk} . The median is $T_{\text{pk}} = 0.6$ K and the cutoff at small T_{pk} is likely due to the sensitivity limit. The arrow represents the $5\Delta T_b$ detection level. We assume \sqrt{N} errors. (b) Histogram of the FWHM of the velocity profile of the clouds, where the median is 12.8 km s $^{-1}$. As the spectral resolution is 0.8 km s $^{-1}$ and all but one linewidth is greater than 3.4 km s $^{-1}$, the linewidths are well resolved. (c) Histogram of the angular size of clouds, $\sqrt{\theta_{\text{maj}}\theta_{\text{min}}}$, where θ_{maj} and θ_{min} are from Table 1. The median angular diameter of the clouds is $29'$, which is approximately twice the beam size. This median, along with the apparent lack of clouds with small angular sizes, is most likely due to the spatial resolution limit ($15'$, denoted by an arrow) and suggests that many of the clouds are unresolved.

provide a uniformly selected sample.

4.1. Derived Properties

The physical properties and positions of the tangent point clouds are presented in Table 2, while descriptions of the derived quantities are presented below.

Columns 1-3: As in Table 1.

Column 4: The deviation velocity, $V_{\text{dev}} = V_{\text{LSR}} - V_t$ (Wakker 1991), where V_t is the most negative velocity expected from Galactic rotation in the fourth quadrant, in km s $^{-1}$, and was determined by McClure-Griffiths & Dickey (2007) from H I observations for $l \leq 339.695^\circ$ and by Luna et al. (2006) from CO observations for all remaining longitudes.

Column 5: The distance, d , along the line-of-sight from the Sun to the cloud determined by assuming the cloud is at the tangent point: $d = R_0 \cos l / \cos b$, in kpc.

Column 6: The Galactocentric radius, $R = R_0 |\sin l|$, of the tangent point at the cloud's location, in kpc.

Column 7: The height, z , of the cloud from the plane of the Galaxy, determined geometrically to be $z = d \sin b$, in kpc.

Column 8: The radius, r , of the cloud in pc, determined by $\sqrt{r_{\text{maj}}r_{\text{min}}}$, where $r_{\text{maj}} = (1/2)d\theta_{\text{maj}}$, $r_{\text{min}} = (1/2)d\theta_{\text{min}}$, and θ_{maj} and θ_{min} are from Table 1.

Column 9: The physical mass of H I in the cloud, M_{HI} , determined as in Column 8 of §3.2 but with the tangent point distance assumed, in M_\odot .

4.2. Uncertainties in Derived Properties

Here we present error estimates for the derived properties in Table 2.

δV_{LSR} : As in Table 1.

δV_{dev} : This error is $\sqrt{\delta V_{\text{LSR}}^2 + \delta V_t^2}$, where $\delta V_t = 3$ km s $^{-1}$ for clouds located at longitudes where V_t was determined using H I ($l \leq 339.695^\circ$; McClure-Griffiths & Dickey 2007). For all other longitudes, where the terminal velocity was determined using CO observations (Luna et al. 2006), the error is assumed to be 9 km s $^{-1}$, as suggested from the scatter on Figure 7 of McClure-Griffiths & Dickey (2007).

δd : Distance errors, which are inherent to the assumption that the clouds are located at tangent points, were estimated using a simulated population of clouds (see §5.3).

δR : The error on the Galactocentric radius was determined analogously to δd . Because the closest point to the Galactic center along a given line-of-sight is the tangent point, the adopted R is always a lower limit and the error can only be positive.

δz : The error on the height is estimated to be $\delta d |\sin b|$.

δr : The error on the radius of the cloud depends on the uncertainties in the distance and angular size estimates and is $\delta r = r \sqrt{(\delta\theta/\theta)^2 + (\delta d/d)^2}$, where $\theta = \sqrt{\theta_{\text{maj}}\theta_{\text{min}}}$

and $\delta\theta = (1/2)\sqrt{\delta\theta_{\text{min}}^2(\theta_{\text{maj}}/\theta_{\text{min}}) + \delta\theta_{\text{maj}}^2(\theta_{\text{min}}/\theta_{\text{maj}})}$.

δM_{HI} : The error on the mass is $M_{\text{HI}} \sqrt{(\delta M_{\text{HI}} d^{-2} / M_{\text{HI}} d^{-2})^2 + (2\delta d/d)^2}$, where $M_{\text{HI}} d^{-2}$ is given in Table 1.

5. ANALYSIS OF THE TANGENT POINT CLOUD POPULATION

5.1. Simulated Halo Cloud Population

To constrain the spatial and kinematic properties of the observed tangent point cloud population we simulated a population of clouds to which were applied the same l , b and V_{LSR} selection criteria as for the GASS pilot region clouds. The simulated clouds were randomly sampled from the following distribution:

$$n(R, z) = \Sigma(R) \exp\left[-\frac{|z|}{h}\right], \quad (1)$$

where $\Sigma(R)$ is the radial surface density distribution, h is the exponential scale height and R and z are the cylindrical coordinates. $\Sigma(R)$ is composed of 12 independent radial bins of width 0.25 kpc, spanning $R = 2.5$ to 5.5 kpc. The amplitude of each bin was optimized to best fit the observed longitude distribution of the tangent point clouds by minimizing the Kolmogorov-Smirnov (K-S) D statistic (the maximum deviation between the cumulative distributions) using Powell's algorithm (Press et al. 1992). We optimized the fits using three different initial estimates on $\Sigma(R)$. All converged on a similar solution and we adopted the mean of the three as the best fit to the data, which is shown in Figure 9.

Velocities of simulated clouds were based on a flat rotation curve where $\Theta = \Theta_0$ with a random velocity component drawn from a Gaussian of dispersion

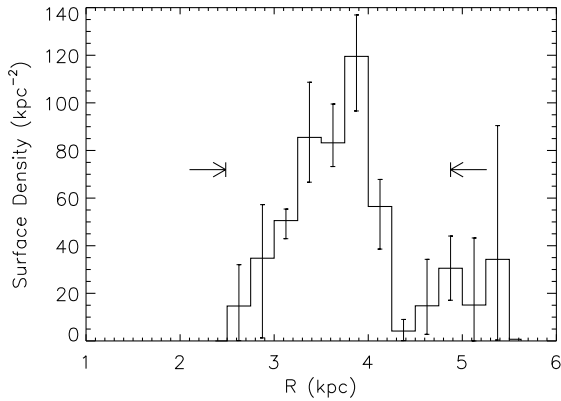


FIG. 9.— Best estimate of the radial surface density, $\Sigma(R)$, of clouds in the GASS pilot region. Error bars denote the range in amplitude within each bin for the three radial solutions. Clouds were detected at all longitudes within the GASS pilot region, where corresponding tangent point boundaries in R are indicated by arrows. The distribution suggests that the clouds are concentrated in radius, peaking at $R = 3.8$ kpc.

$\sigma_{cc} = 18 \text{ km s}^{-1}$, which is discussed in detail in §5.2. We generated 5×10^4 clouds in a half-galaxy (third and fourth quadrants), of which 2475 were within the Galactic coordinates of the GASS pilot region and also within the defined velocity range of the tangent point cloud sample. We then normalized this distribution to compare directly with the observed distribution. We performed K-S tests to estimate the quality of the fit between the observed and simulated distributions. Based on these tests, we find that the parameters of the simulated population reproduce the distribution of observed tangent point clouds well and are therefore good estimates for those of the intrinsic population. Results of the fits to the distributions are presented in §5.2–5.5 along with tests of other functional forms.

5.2. Cloud-to-Cloud Velocity Dispersion

We assume that a random cloud-to-cloud velocity dispersion (σ_{cc}) is responsible for the presence of clouds at forbidden velocities within the GASS pilot region. Simulations of the global cloud population were required to model the effects of these motions, which can cause clouds that are not located at tangent points to have velocities that are near or beyond V_t . The cloud-to-cloud velocity dispersion can provide information on the expected scale height of the distribution and a better understanding of the formation mechanisms of the clouds. We find the V_{dev} distribution of the tangent point sample of clouds to be consistent with that derived from a Gaussian distribution of random velocities whose dispersion is $\sigma_{cc} = 18 \text{ km s}^{-1}$, with a K-S test probability greater than 97%⁸. These distributions are presented in Figure 10, where the simulated V_{dev} distribution is represented by a dashed line and the observed distribution by a solid line. Velocity dispersions of 16 to 22 km s^{-1} also provide acceptable fits (K-S test probabilities greater than or equal to 15%), as do fits where the random velocity component is drawn from an exponential distribution rather than a Gaussian distribution (with a K-S test probability

⁸ For reference, a 97% probability is roughly equivalent in confidence to a 0.04σ detection of a difference, i.e., no detectable difference in the distributions, 15% corresponds to 1.4σ , and 1% corresponds to 2.6σ .

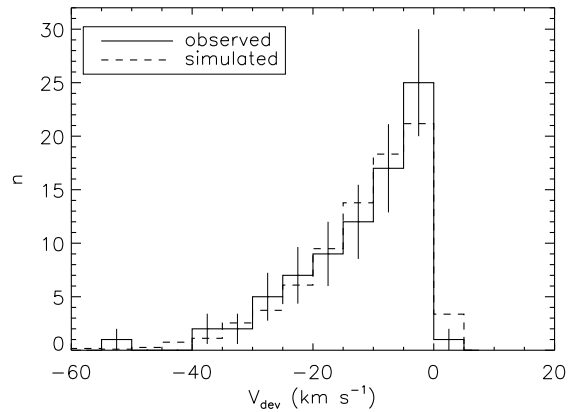


FIG. 10.— Distribution of deviation velocities of the observed tangent point and simulated population of clouds, where the simulated clouds are normalized to the same total number of observed tangent point clouds. Observed clouds are represented by a solid line, while simulated clouds are represented by a dashed line. To reduce the effects of small number statistics, simulations were run with 5×10^4 clouds. We assume \sqrt{N} errors.

of 89% for a scale velocity of 13 km s^{-1}). The implied kinematics of the cloud population based on this result are discussed in §6.1.

Estimating the uncertainties on our determined σ_{cc} is extremely difficult. We expect these uncertainties to be coupled to errors introduced by the measurements of V_t , which are difficult to untangle due to the possibility that random motions can systematically offset the measured V_t . Another possible source of uncertainty is streaming motions associated with spiral features. However, because V_t was determined directly from H I and CO measurements rather than from a fitted rotation curve, streaming motions should already be reflected in the adopted V_t .

5.3. Distances Errors

The simulations allow us to estimate the error in our assumption that clouds with $V_{\text{dev}} \leq 0.8 \text{ km s}^{-1}$ are at the tangent point. We have calculated the fractional distance error of the simulated clouds as a function of deviation velocity within a 5 km s^{-1} wide V_{dev} bin (Figure 11). Clouds at increasingly forbidden velocities have smaller distance errors, i.e., are more likely to be near the tangent point; the degree to which this is true depends on the magnitude of σ_{cc} . We also calculated the fractional distance error as a function of longitude and found that clouds with longitudes corresponding to the Galactocentric radii where few clouds are detected ($l \sim 328^\circ$) have larger distance errors (this is expected because few clouds are intrinsically at these radii and therefore a larger fraction of the forbidden velocity clouds at these longitudes are likely interlopers from larger radii). We assume that the errors due to V_{dev} and longitude are independent. The adopted fractional distance error is the product of the fractional distance error due to V_{dev} (relative to the typical error of 0.12), due to longitude (relative to the typical error) and the typical error itself. The fractional distance errors due to V_{dev} and longitude are taken to be the rms error for the simulated clouds within the same bin. We have confirmed that the fractional distance error of the simulated clouds does not significantly depend on their latitude. Based on the relative distance errors, we believe that our assumption that clouds with

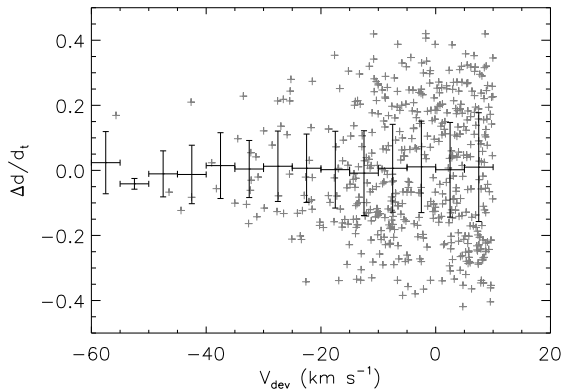


FIG. 11.— Relative distance error as a function of deviation velocity (crosses) for a population of simulated clouds. Clouds with a large forbidden velocity (i.e., large negative value of V_{dev}) are more likely to be at the tangent point and thus have smaller errors in their estimated distances. These points have been placed into bins of width 5 km s^{-1} , denoted by the horizontal bars, and the vertical error bars denote the mean and standard deviation of the distribution within each bin. Approximately one fifth of simulated points are displayed here but the error bars have taken all simulated data into account. The left most error bar is large due to small number statistics.

$V_{\text{dev}} \leq 0.8 \text{ km s}^{-1}$ are located near their tangent point is reasonable.

5.4. Radial Distribution

The adopted radial distribution of the tangent point clouds along with that of the simulated population of clouds is shown in Figure 12. The apparent offset in the distributions results from the assumption that the forbidden velocity clouds are located at tangent points, which are always at the smallest value of R along the line of sight.

Another useful quantity that can be extracted from the simulations is the mean radial surface density distribution of clouds within the GASS pilot region (Figure 9). Although clouds are observed at all longitudes within the GASS pilot region, the distribution is concentrated in Galactocentric radius and peaks at $R = 3.8 \text{ kpc}$. The error bars at $R \gtrsim 5 \text{ kpc}$ are significantly larger because clouds at these radii must have large random velocities in order to meet the sample criteria and therefore represent a small tail of the population. With a K-S test probability of 95%, the simulated longitude distribution fits that of the observed distribution of the tangent point sample well (Figure 13a).

The number of clouds in a uniformly distributed population of tangent point clouds should monotonically decrease by a factor of ~ 2 between $l = 325^\circ$ and $l = 343^\circ$, as demonstrated by Equation (A2) in Stil et al. (2006), where they show that the line-of-sight distance effectively surveyed over forbidden velocities is $\Delta d = \sqrt{8R_0} |\sin l| \sqrt{\sigma_{cc}/\Theta_0} \propto |\sin l|$. We have overlaid the distribution of a uniform surface density population in Figure 13a and it is clear that it is in stark contrast to the centrally peaked longitude distribution we observe. We therefore conclude that the peaked radial distribution is real. In Figure 13b we present the longitude distributions of the simulated and observed clouds within the entire pilot region, i.e., at all $-200 \leq V_{\text{LSR}} \leq -70 \text{ km s}^{-1}$. Even though the vast majority of these clouds were not used to constrain the simulated radial distri-

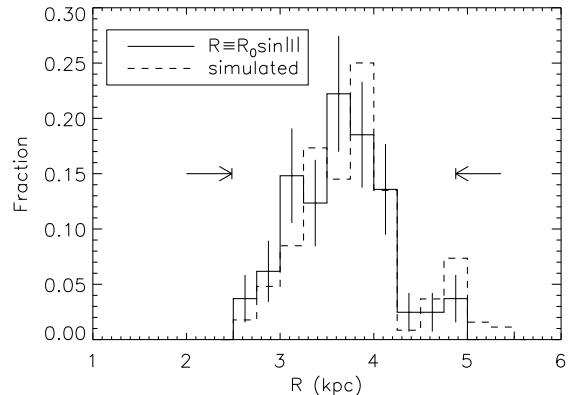


FIG. 12.— Histogram showing the fraction of the sample located at each Galactocentric radius. The solid line denotes the clouds assumed to be located at tangent points and the dashed line denotes the corresponding simulated radial distribution (dashed line). The shift between the simulated and adopted radial distributions results from systematic errors that stem from the assumption that the forbidden velocity clouds are located at tangent points, i.e., at the minimum possible value of R . Arrows represent the radial boundaries of tangent points within the GASS pilot region. We assume \sqrt{N} errors.

bution, their longitude distribution is well reproduced. The tangent point sample therefore appears to be a fair representation of the entire GASS pilot region.

It is worth investigating whether our assumptions regarding the functional form of the velocity distribution affects the inferred radial distribution, i.e., could a distribution with more velocity outliers and a less strongly peaked radial distribution also fit the data? To test this we have performed the same optimization of the radial distribution while using an exponential velocity distribution. We find that the resulting radial profile is identical to within the errors, confirming the robustness of this result.

5.5. Vertical Distribution

The vertical distribution of both the tangent point and simulated cloud population is presented in Figure 14. Clouds have been detected throughout the entire range of latitudes covered by the GASS pilot region, up to corresponding heights of $|z| = 2.5 \text{ kpc}$. However, there are very few clouds at $|b| \leq 2.5^\circ$ because identification of clouds was extremely difficult close to and within the Galactic plane, except in cases where clouds were observed at large forbidden velocities. Because of this incompleteness at low latitudes, we compare the latitude distributions of simulated and observed clouds with $|b| > 2^\circ$ and find that they are consistent for vertical scale heights between $400 - 500 \text{ pc}$, with K-S test probabilities of at least 25%. As incompleteness may still be a problem at $|b| \approx 2^\circ$, we also compare the height distributions for only clouds at $|b| > 3^\circ$ and find acceptable fits for scale heights between 300 and 400 pc , both with probabilities greater than 50%. Based on these comparisons we conclude that the population is best represented with a exponential scale height of $h = 400 \text{ pc}$. A $\text{sech}^2(z/z_0)$ distribution with $z_0 = 700 \text{ pc}$ provides an equally good fit the the data, which is not surprising given that the exponential and sech^2 distributions differ primarily near $z = 0 \text{ pc}$ where we cannot constrain the fit.

Although incomplete, the combination of surface density, mean mass and scale height of the clouds gives

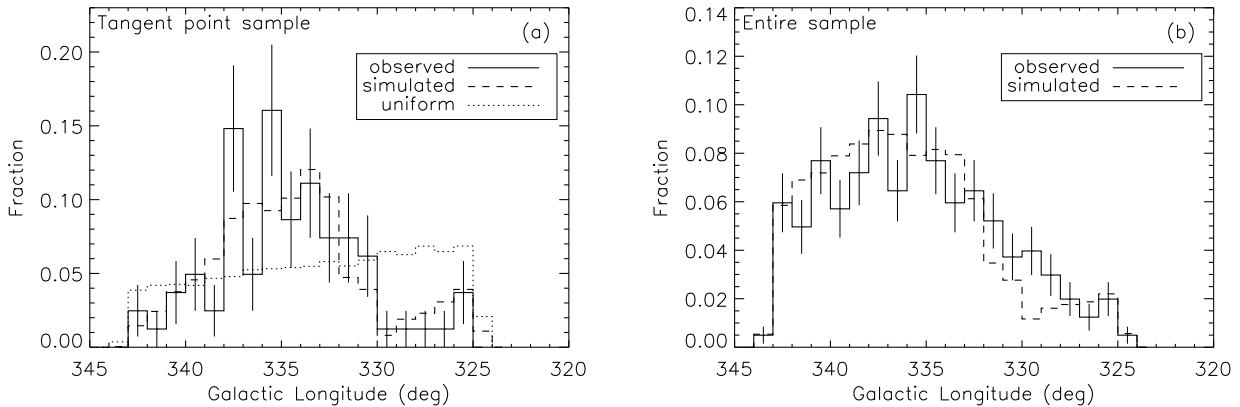


FIG. 13.— (a) Histogram presenting the longitude distribution of the observed tangent point clouds (solid line) and corresponding simulated distribution (dashed line), along with the distribution expected from a uniform population (dotted line). There is a peak in the observed and simulated distribution, which is clearly different from that expected of a uniform population. (b) Histogram presenting the longitudes of all clouds detected in the GASS pilot region (solid line) along with the corresponding simulated population (dashed line). The distributions are similar, suggesting that the tangent point sample represents the pilot region fairly well. We assume \sqrt{N} errors.

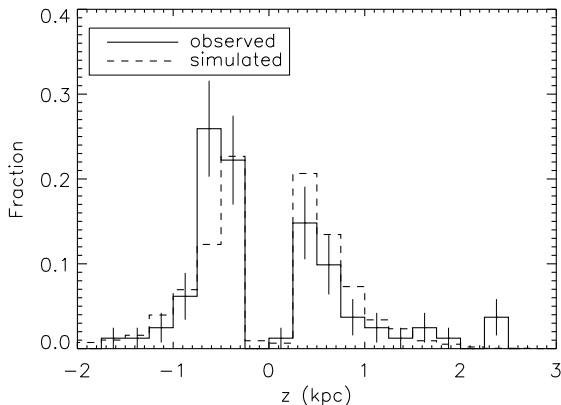


FIG. 14.— Histogram of the fraction of the observed (solid line) and simulated (dashed line) clouds as a function of height. The lack of observed clouds at low $|z|$ is a selection effect due to confusion. This effect was taken into account during comparisons with the simulated population by omitting all simulated clouds with $|b| \leq 2^\circ$. The exponential scale height of the distribution is $h = 400$ pc. We assume \sqrt{N} errors.

a rough estimate of the vertical distribution of H I contributed by the cloud population. The mid-plane H I number density can be estimated by $n(0) = \Sigma(R) \langle M \rangle / (2hM_{\text{H}})$, where $\langle M \rangle$ is the mean cloud H I mass and M_{H} is the H I atom mass. We find that the clouds are responsible for $\sim 5\%$, by H I number density, of the exponential component of the H I layer in Dickey & Lockman (1990) and have a very similar scale height.

We note that there is an asymmetry in the number of observed clouds above and below the disk at $|z| \leq 750$ pc and an excess of clouds at large positive latitudes. Possible explanations for these are discussed in §6.

5.6. Physical Size and Mass

Cloud radii, r , vary from ~ 15 pc to 65 pc, with a median radius of 32 pc, as can be seen in Figure 15a. The angular resolution of the telescope sets a lower limit on the observed cloud size. The maximum angular extent of the detected clouds suggests that roughly 80% of the entire sample is unresolved in at least one dimension. Derived radii should therefore be thought of as upper limits. A histogram of the H I mass of the clouds at tangent points is presented in Figure 15b, demonstrating that the

clouds range in size from hundreds to thousands of solar masses, with a median H I mass of $630 M_{\odot}$. These values may be overestimates if confusion is significant.

5.7. Comparison of GASS Clouds to Lockman Clouds

Based on their angular sizes and location in the lower halo, the clouds detected in the GASS pilot region appear to be similar to those observed by Lockman (2002). We investigate this possibility further by comparing the properties of each distribution summarized in Table 3. The median Δv is strikingly similar in both sets of data, which is not surprising if the clouds are part of the same population. The derived σ_{cc} are also in agreement. The median $|z|$ of this sample is smaller than that of Lockman (2002) but this is most likely due to a selection effect, as the areas searched by Lockman (2002) tended to be further from the Galactic plane to avoid areas of confusion. The most obvious differences in the sample stem from the difference in the angular resolutions of each survey: $15'$ for GASS data versus $9'$ for the GBT data. This affects T_{pk} , N_{HI} , and r , where T_{pk} and N_{HI} would naturally be lower for unresolved clouds, and r would be larger. If confusion is important, M_{HI} would also be larger. Lockman (2002) estimated that 25% of the clouds were unresolved while we have estimated $\sim 80\%$ here. The clouds observed by Lockman (2002) are much less massive, with approximately one third having $M_{\text{HI}} \leq 30M_{\odot}$, while none of the observed GASS clouds have masses that low. As the only differences in the observed properties are due to differences in the observations, these comparisons reveal that the clouds belong to the same population of clouds as those detected by Lockman (2002).

5.8. Observed Trends

There does not appear to be any correlation between the height of the clouds and V_{LSR} , R , or r . However, as the data in Figure 16 suggest, there may be a trend between Δv and $|z|$, where clouds near the plane ($|z| \leq 1$ kpc) have a median FWHM of 10 km s^{-1} and a large dispersion, where as those at $|z| > 1$ kpc have a median FWHM of 17 km s^{-1} and a smaller dispersion. One possible explanation for such a trend could be that the clouds at larger heights belong to a different population of clouds than those at lower heights. Another possi-

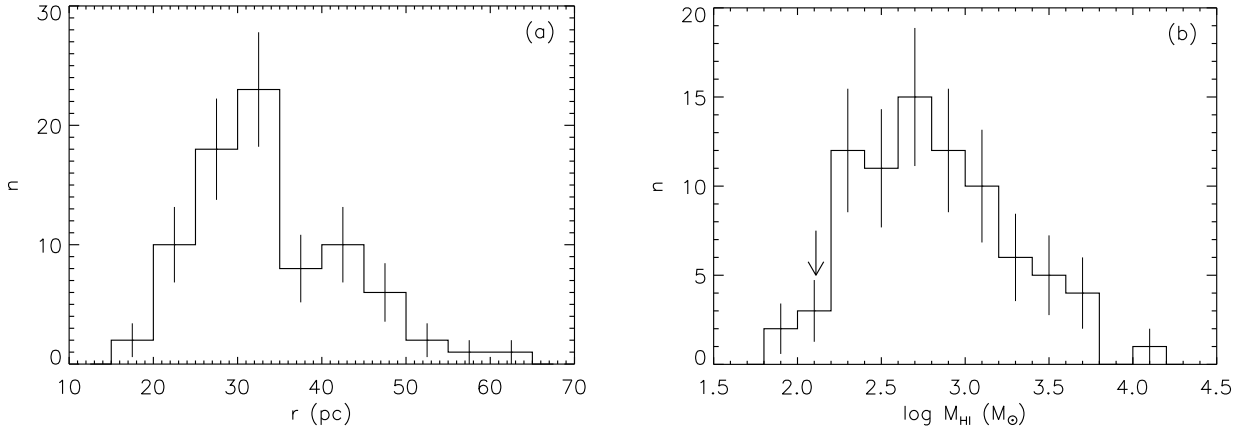


FIG. 15.— (a) Histogram of the physical radius of clouds at tangent points. The median $r = 32$ pc. The cutoff at small radii is a result of the spatial resolution limit. (b) Histogram of $\log M_{HI}$ of clouds at tangent points. The $\sim 5\Delta T_b$ limit is represented by an arrow for a cloud with the median $r = 32$ pc. We assume \sqrt{N} errors.

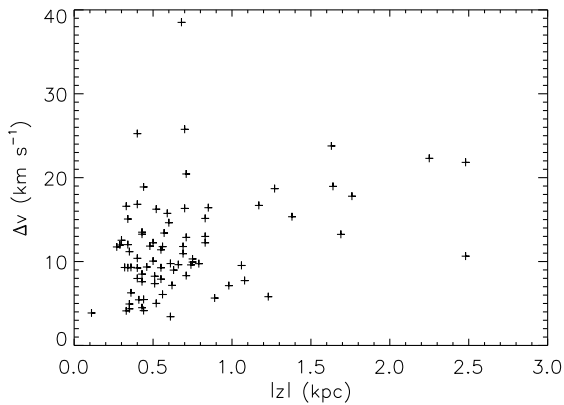


FIG. 16.— FWHM of the velocity profile, Δv , of the tangent point clouds as a function of height. Clouds at larger heights may have larger linewidths.

bility is that if the clouds are in pressure equilibrium, the trend is reflecting pressure variations throughout the halo. Similar to our results, Lockman (2002) found that V_{LSR} and r are independent of z , and also found evidence that clouds with more narrow linewidths lay closer to the plane.

As one might expect if a population of clouds has a narrow range of densities, the larger the radius of the cloud, the more massive it is. This trend is evident in Figure 17 and does not appear to be solely due to the H I mass sensitivity limit of the data. This limit is denoted by the curved line and is based on the minimum observable H I column density, $N_{HI_{min}} = 1.94 \times 10^{18} T_{b_{min}} \Delta v_{med}$ in cm^{-2} , where $T_{b_{min}}$ is the minimum observable T_b (assumed to be $5\Delta T_b$) and Δv_{med} is the observed median Δv .

Another apparent trend, as seen in Figure 18, is that the clouds with higher H I column densities appear to be at lower heights. This could be due to inclusion of unrelated diffuse emission with the clouds at lower heights if the background subtraction was not effective. It could also be explained by a scenario where each cloud was given the same kinetic energy from a formation process or via equipartition in the subsequent evolution of the cloud population. The higher mass clouds, which have higher N_{HI} , would then have preferentially lower velocities and would not reach heights as large as those reached by clouds with higher velocities. Figure 19 provides

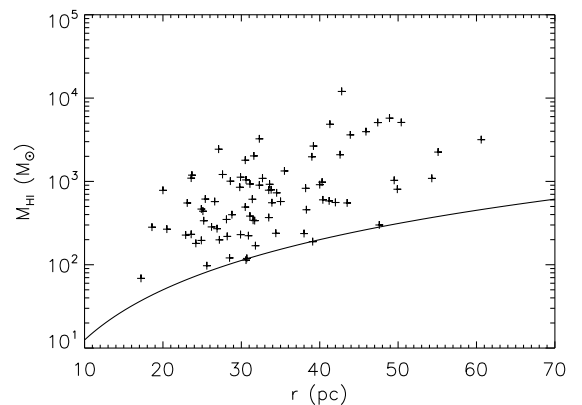


FIG. 17.— Derived H I mass of the clouds as a function of cloud radius (crosses). The curved line represents the lower H I mass limit and is based on the minimum observable N_{HI} . The minimum brightness temperature is assumed to be $5\Delta T_b$. The larger clouds are more massive.

tentative support for this hypothesis, revealing that at $|z| \geq 1$ kpc there are very few clouds with $M_{HI} \geq 10^3 M_\odot$ (note, however, that at these heights our statistics are poor). Lockman (2002) did not find a correlation between the H I column density or mass with height, but this could be due to the limited vertical range of his data. Similarly, a correlation between the H I mass of a cloud and its deviation velocity is suggested in Figure 20; in particular, the more massive clouds may have lower deviation velocities. If the more massive clouds have lower random motions, they could have lower typical deviation velocities. This would be consistent with a scenario in which clouds evolve to an equipartition of energy or in which each cloud is given a similar initial kick, for example, from similar supernovae explosions. This could also explain why all of the most massive clouds are seen closer to the plane (Figure 19): if they have smaller initial velocities, they would not move as far into the halo before falling back towards the plane. At this stage, however, we can not exclude the possibility that at lower heights confusion is affecting the determined H I column density and mass of the clouds. We discuss the kinematics of the cloud population further in §6.1.

6. THE ORIGIN AND NATURE OF HALO CLOUDS

6.1. Kinematics of Halo Cloud Population

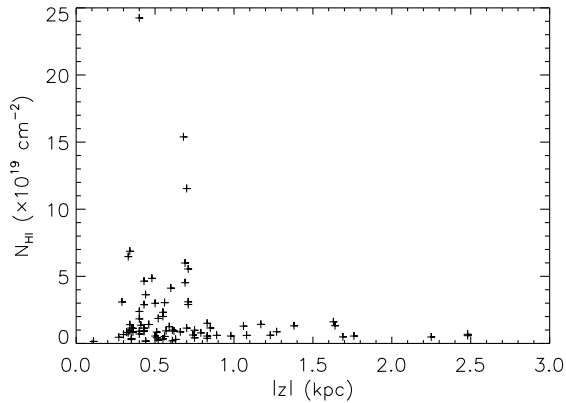


FIG. 18.— H I column density as a function of height. All clouds with large column densities are located at lower heights, i.e., closer to the Galactic disk.

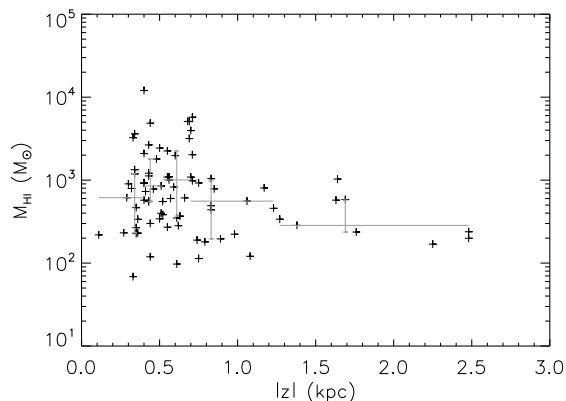


FIG. 19.— H I mass of the clouds as a function of height (crosses). Horizontal lines represent the median M_{HI} per 18 clouds and error bars represent the 25th to 75th percentile range. There is no evidence for a trend until $|z| \sim 1$ kpc, where there may be a lack of massive clouds.

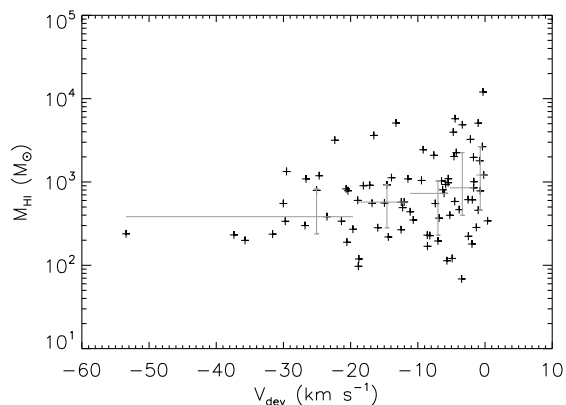


FIG. 20.— H I mass of the clouds as a function of deviation velocity (crosses). Horizontal lines represent the median M_{HI} per 18 clouds and error bars represent the 25th to 75th percentile range. The more massive clouds have lower deviation velocities.

The velocity dispersion of the cloud population is likely a remnant of a common formation process, such as violent supernovae explosions. If the population is in equilibrium, the vertical distribution and velocity dispersion are linked via the potential. By using the simulated population of clouds, we found that the vertical distribution is best fit with an exponential scale height of 400 pc (§5.5) and the V_{dev} distribution is best fit with a Gaussian dis-

persion of $\sigma_{cc} = 18$ km s⁻¹ (§5.2). However, assuming a vertical force using the mass model of Kalberla et al. (2007) at $R = 3.8$ kpc, we derive an exponential scale height of 90 pc for an isothermal population of clouds with $\sigma_{cc} = 18$ km s⁻¹. To produce our observed scale height of 400 pc within this potential, the cloud-to-cloud velocity dispersion would have to be 60 km s⁻¹. The difference between the σ_{cc} required and that observed may be due to the lack of clouds observable in the disk; if a large number of clouds within the disk have gone undetected, the scale height could be lower than 400 pc, and could therefore be explained by the observed velocity dispersion. It is also possible that the distribution cannot be explained by a single component, but this is not obvious in the current data (we will address this possibility in a subsequent paper). However, the magnitude of this difference suggests that the clouds do not belong to an equilibrium population and their heights must, in part, result from processes that do not increase the velocity dispersion, such as uniformly expanding H I shells, instead of bursts of energy from areas of active star formation generating random “kicks.” The clouds could have also originated above the disk, as in a galactic fountain model.

Similar clouds have been detected at forbidden velocities within the Galactic disk using data from the VLA Galactic Plane Survey, suggesting that the clouds are not restricted to the halo (Stil et al. 2006). Those cloud diameters are much smaller than the ones derived here (they have diameters ~ 10 pc), likely due to the higher spatial resolution of the VLA data. Based on their models, Stil et al. (2006) find that a vertical Gaussian half-width at half-maximum (HWHM) larger than 1 kpc (equivalent to an exponential scale height of 1.2 kpc) best fits their data, but given that they only surveyed within $|b| \leq 1.3^\circ$, this is likely to be strongly affected by the lack of coverage at high latitudes, especially because we observe similar clouds up to $|z| = 2.5$ kpc and Lockman (2002) has observed clouds up to ~ 1.5 kpc. Stil et al. (2006) find a lower limit to the HWHM of the clouds to be 180 pc (exponential scale height of 216 pc), which is consistent with the value we derive and also inconsistent with the value expected for the derived velocity dispersion.

It is worth noting that there is evidence that similar clouds may also be abundant in the outer Galaxy (Stanimirović et al. 2006). It is not yet certain whether they belong to the same population of clouds, but with larger surveys of H I clouds in the lower halo of the Galaxy, such as those presented here and in the entire inner Galaxy within GASS, along with those underway by the Galactic Arecibo L-Band Focal Plane Array Consortium and other groups, properties such as σ_{cc} and the spatial distribution can be determined more accurately and will therefore help constrain the kinematics and formation mechanisms of the clouds.

6.2. Halo Clouds and Spiral Structure

As discussed in §5.4, the surface density of halo clouds is not uniformly distributed but instead peaks at a Galactocentric radius of $R = 3.8$ kpc and the population is concentrated in radius. This confined nature suggests that the halo clouds are related to the spiral structure of the Galaxy. Although distances to spiral arms are currently

not well constrained, the location of the peaked radial distribution of the clouds indicates that they may be related to the expanding “3 kpc” arm (van Woerden et al. 1957; Rougoor & Oort 1960), which is tangential to an observer’s line-of-sight at roughly $l = 336^\circ$ (Bronfman 2008; see also Vallée 2008 who argues that this feature lies at $l \sim 339^\circ$ and is the start of the Perseus arm, distinct from the 3 kpc–Norma arm), corresponding to $R = 3.5$ kpc. Also, it has been suggested that the 3 kpc arm must be confined to an annulus of less than 1 kpc in extent (Lockman 1981), which corresponds well with the radial concentration of clouds. At this time, however, the possibility that these clouds are instead related to other Galactic structures such as the “5 kpc molecular ring” (Jackson et al. 2004) cannot be ruled out. This “ring” is likely not a coherent structure but instead a complex region where multiple spiral arms originate (Vallée 2008).

The apparent association between many of the H I clouds and filamentary structures within the GASS pilot region suggests that the clouds are related to star formation because such structures are common in areas of significant supernova activity or stellar winds (Dickey & Lockman 1990). Figure 21 displays an integrated intensity map with many clouds that are clearly aligned along filaments and loops, reminiscent of the clouds observed to be associated with the cap of a superbubble by McClure-Griffiths et al. (2006). Recently, proper motion measurements of the molecular cloud NGC 281 West, which is associated with an H I loop, revealed that the cloud is moving away from the Galactic plane at $20 - 30$ km s $^{-1}$ (Sato et al. 2007). This velocity is similar to our observed velocity dispersion and further supports the scenario that the clouds are related to expanding shells. In this scenario, violent supernovae and stellar winds may have pushed H I from the disk up into the halo or the clouds may be fragments of H I shells (Mac Low et al. 1989; McClure-Griffiths et al. 2006), rather than a result of a standard galactic fountain. In the galactic fountain model hot gas rises from the disk, cools and condenses, then falls back to the plane (Shapiro & Field 1976; Bregman 1980). This would result in a more uniform radial distribution of clouds (Bregman 1980), while we clearly observe a peak in the radial distribution of the clouds that may be associated with the 3 kpc arm. If the halo clouds are related to star formation, the asymmetry in the number of detected clouds at low heights ($|z| \leq 750$ pc) could be a result of this, as any asymmetry in the structure of the ISM and the location of star forming regions may be reflected in the distribution of clouds, and there appears to be more filaments below than above the Galactic plane in the GASS pilot region.

If the clouds are related to spiral structure and star formation then we would expect to see a correlation between the radial surface density distribution of the H I clouds and that of Galactic H II regions. We compare these distributions, along with the mass surface densities of H I and H $_2$, in Figure 22. The mass surface densities have been averaged over the entire Galaxy and were derived by Dame (1993) using H I data from Dickey & Lockman (1990) and Burton & Gordon (1978), and H $_2$ data from Bronfman et al. (1988), whereas the halo cloud distribution from this study includes only the GASS pilot region. The H II regions are taken from Paladini et al.

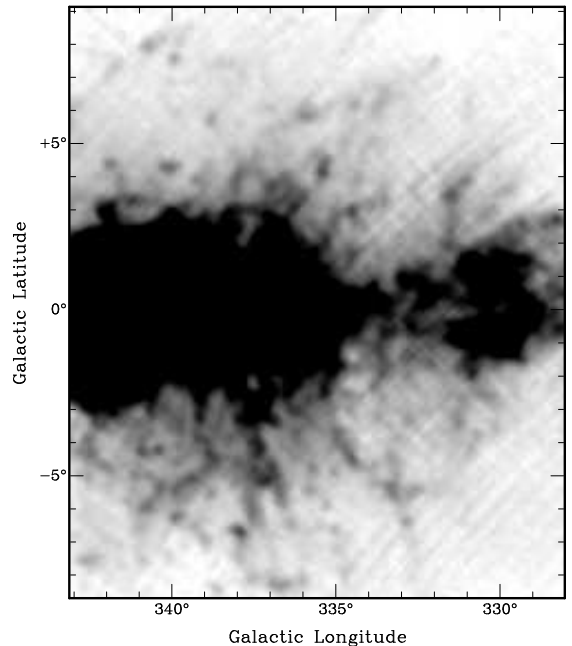


FIG. 21.— Filamentary structures are plentiful within the GASS pilot region, as demonstrated in this longitude–latitude integrated intensity map over $-135 \leq V_{\text{LSR}} \leq -120$ km s $^{-1}$. Many H I clouds in the GASS pilot region are aligned with these loops and filaments, suggesting that they are related to expanding superbubbles or other structures common in areas of star formation. The diagonal striations are instrumental artifacts.

(2004). There is no obvious relationship between the H I cloud and H II region distributions or between the H I clouds and the H I and H $_2$ surface densities, providing conflicting evidence for the relationship between the H I clouds and current star formation. As the evaporation timescale for a cold cloud in a hot medium is expected to be much longer than other timescales associated with cloud evolution (Cowie & McKee 1977; Nagashima et al. 2006), and if evaporation is the main disruptive mechanism, the clouds are long-lived. It is therefore possible that the clouds are tracing past rather than current star formation. With the present data we are only able to make a preliminary study of the relationship between the halo cloud distribution and spiral structure and star formation in the Galaxy. Future analysis of clouds over a larger range of longitudes will allow us to test the assertion that the clouds are related to star formation in greater detail.

6.3. Possible Association with High Velocity Cloud Complex L

An excess of clouds at large positive heights can be seen in the vertical distribution of the clouds (Figure 14); 9% of the clouds at positive heights lie at $z \geq 2$ kpc while none of the clouds below the plane are seen at such heights, and many of them have unusually large deviation velocities (Figure 7). This excess could have several possible origins including infalling gas, increased disk activity on one side of the disk that has resulted in outflowing gas reaching larger heights, or small number statistics. Given the proximity of high velocity cloud complex L to the halo clouds in the upper portion of the GASS pilot region, we compared the H I associated with each population to determine whether or not the presence

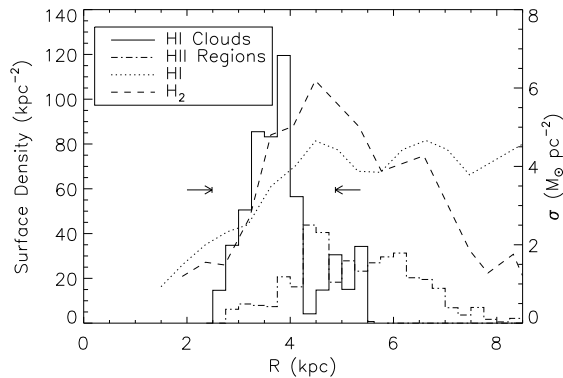


FIG. 22.— Radial surface density distribution of the simulated GASS pilot region H I clouds (solid histogram) and H II regions (scaled up by a factor of 7 for ease of comparison and shown by the dash-dot histogram; Paladini et al. 2004). Mass surface densities of the average Galactic H I (dotted line) and Galactic H₂ (dashed line) are overlaid and were both determined by Dame (1993) using data from Dickey & Lockman (1990) and Burton & Gordon (1978) for H I and data from Bronfman et al. (1988) for H₂. Arrows indicate limits of R for tangent points in the GASS pilot region. The peaked distribution of halo clouds does not appear to be similar to that of the H II regions nor the H I and H₂ mass surface densities, suggesting that the halo clouds are not directly related to current star formation.

of complex L could be responsible for the observed excess.

Complex L was first described by Wakker & van Woerden (1991) to have velocities ranging from $-190 \lesssim V_{\text{LSR}} \lesssim -85 \text{ km s}^{-1}$, longitudes ranging from $341^\circ \leq l \leq 348^\circ$ and latitudes ranging from $31^\circ \leq b \leq 41^\circ$, and they speculated that the clouds were part of a population that was related to a galactic fountain. Since then, H α distance limits have been determined for complex L, placing it within the Galactic halo at heights of $4 \leq z \leq 12 \text{ kpc}$ from the plane and heliocentric distances of 8 to 22 kpc (Weiner et al. 2001; Putman et al. 2003).

In Figure 23 we display a region of the GASS data that encompasses both the upper GASS pilot region, outlined by the solid black lines, and the lower velocity gas of complex L. We have overlaid circles on high velocity clouds associated with complex L as catalogued by Wakker & van Woerden (1991), regardless of their velocity. The spatial morphology of the H I at velocities where gas is detected in complex L suggests that there is a connection between the clouds in the GASS pilot region and those in complex L, in the form of a filamentary structure that is contiguous in velocity and connects complex L with the disk. Also, with the assumption that the halo clouds at large positive latitudes are located at tangent points, their heights are between $1.5 \leq z \leq 2.5 \text{ kpc}$ with distances $\sim 8 \text{ kpc}$, which place them in the vicinity of the lower height estimates of complex L. These correlations suggest that complex L may have similar origins as the clouds presented here and it may be responsible for the observed excess of clouds at large positive latitudes.

6.4. Stability of Halo Clouds

The amount of mass required for a spherical cloud to be gravitationally bound is $M \approx r\Delta v^2/G$, where r is the radius of the cloud, Δv is the linewidth of its velocity profile and G is the gravitational constant. For a cloud with $r = 32 \text{ pc}$ and $\Delta v = 12.8 \text{ km s}^{-1}$, the median observed values, this would require a mass on the order

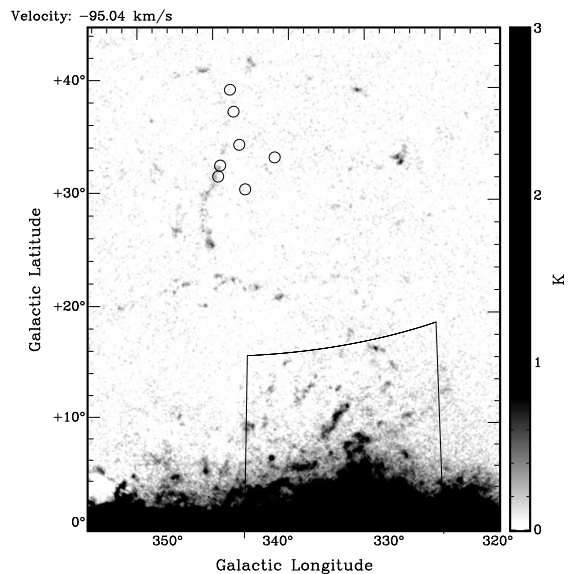


FIG. 23.— GASS data encompassing the upper portion of the GASS pilot region, outlined by the solid black lines, along with the high velocity cloud complex L. Circles have been placed at the positions of high velocity clouds within complex L, regardless of their V_{LSR} , as determined by Wakker & van Woerden (1991). The morphology of the H I in the upper GASS pilot region, in complex L, and between them, suggests that complex L may have similar origins as the observed halo clouds and may be responsible for the observed excess of clouds at large positive latitudes.

of $10^6 M_\odot$. As none of the detected clouds have masses this large, they are either pressure confined or transitory.

Because turbulence also contributes to the linewidths, an upper limit for the thermal pressure within the clouds is $P = nT \leq 22 \langle n \rangle \Delta v^2$, in units of K cm^{-3} , where $\langle n \rangle$ is the average number density and T is the thermal temperature. However, as $\langle n \rangle$ is a lower limit and T is an upper limit, and $\langle n \rangle$ and T are uncorrelated, we are unable to put any constraints on the pressure of these clouds with the present data. It is possible that pressure changes are responsible for the observed trend in Figure 16, which tentatively shows that clouds further from the disk of the Galaxy have larger linewidths. If the clouds are in pressure equilibrium, their pressures could provide us with insight into the pressure structure of the halo, which is currently not well understood.

7. SUMMARY

We have detected over 400 H I clouds in the lower halo of the Galaxy in the Galactic All-Sky Survey pilot region. These clouds have a median peak brightness temperature of 0.6 K , a median velocity width of 12.8 km s^{-1} , and angular sizes $\lesssim 1^\circ$. As these clouds follow Galactic rotation, a subset was selected that is likely to be located at tangent points of the inner Galaxy, allowing us to determine their distances and therefore their sizes and masses. The tangent point clouds have radii on the order of 30 pc and a median H I mass of $630 M_\odot$. The properties of these clouds suggest that they belong to the same population of clouds discovered by Lockman (2002).

We simulated the population of clouds to constrain their random cloud-to-cloud velocity dispersion, σ_{cc} , and spatial distribution. We found that $\sigma_{cc} = 18 \text{ km s}^{-1}$, but if the clouds were left to evolve in the Galactic potential without any disruptions, these random motions would produce a scale height of 90 pc , which is inconsistent

with our derived scale height of 400 pc. This suggests that the clouds do not belong to an equilibrium population. We detected clouds throughout the entire GASS pilot region, up to the latitude boundaries ($|b| \lesssim 20^\circ$). Few clouds were observed at low latitudes due to confusion, which may have resulted in an underestimate of the number of clouds at low heights, and therefore an overestimate in the derived scale height.

Our large, homogeneously-selected sample has allowed us to determine the spatial distribution of these halo clouds for the first time and has revealed that although clouds were observed at all longitudes within the GASS pilot region, they do not appear to be uniformly distributed but instead are concentrated in radius, peaking at $R = 3.8$ kpc. We analyzed this distribution and suggest that the clouds are related to the spiral structure of the Galaxy. In particular, the peak in the radial distribution is suggestive of a relation to the 3 kpc arm. This relation to a specific spiral feature remains speculative until further analysis using a larger sample of clouds and better constrained spiral structure models can be performed. It is therefore unlikely that the halo clouds are a result of a standard galactic fountain, as radial enhancements would not be expected in this scenario (Bregman 1980). Instead, it appears that the clouds may be directly related to areas of active star formation, in the form of fragmenting H I shells and H I gas that has been pushed into the halo. This is further supported by the appearance of numerous clouds related to filaments and loops, whose structures may have resulted from stellar winds and supernovae (Dickey & Lockman 1990). However, a comparison between the radial surface density distribution of H I clouds and H II regions provides conflicting

evidence: if clouds are related to areas of star formation, a relationship between the clouds and H II regions would be expected but is not observed.

The morphology of H I at large positive latitudes in the GASS pilot region suggests that some of the clouds may be related to high velocity cloud complex L, whose lower height estimates of 4 kpc and distance estimates of 8 kpc place it in the vicinity of the clouds presented here. If they are related, it is possible that whatever process is responsible for the halo clouds, e.g., star formation, is also responsible for complex L. This is further supported by recent observations of IVCs, which suggest that the IVCs are related to energetic events in the Galactic disk and that they are likely linked to spiral structure (Kerton et al. 2006). The majority of those IVCs have $V_{\text{dev}} \leq 20$ km s $^{-1}$, implying a Galactic origin, and we suggest that they are similar to the cloud population presented here.

A future study of halo clouds within the entire inner Galaxy observed by the Galactic All-Sky Survey will provide a much larger sample of tangent point clouds, enabling more complete statistics for distribution studies and a better understanding of Galactic structure. These studies will include comparisons between the distribution of halo clouds and that of tracers of star formation, such as H II and H $_2$, and will allow us to better constrain the origin of these clouds.

The Parkes Observatory is operated by the Australia Telescope National Facility, a division of the Commonwealth Scientific and Industrial Research Organisation.

Facilities: Parkes ()

REFERENCES

- Barnes, D. G. et al. 2001, MNRAS, 322, 486
 Bregman, J. N. 1980, ApJ, 236, 577
 Bronfman, L. 2008, Ap&SS, 313, 81
 Bronfman, L., Cohen, R. S., Alvarez, H., May, J., & Thaddeus, P. 1988, ApJ, 324, 248
 Burton, W. B., & Gordon, M. A. 1978, A&A, 63, 7
 Cowie, L. L., & McKee, C. F. 1977, ApJ, 211, 135
 Dame, T. M. 1993, in American Institute of Physics Conference Series, Vol. 278, Back to the Galaxy, ed. S. S. Holt & F. Verter, 267
 de Avillez, M. A. 2000, MNRAS, 315, 479
 Dickey, J. M., & Lockman, F. J. 1990, ARA&A, 28, 215
 Ferrière, K. M. 2001, Reviews of Modern Physics, 73, 1031
 Heiles, C. 1967, ApJS, 15, 97
 —. 1979, ApJ, 229, 533
 —. 1990, ApJ, 354, 483
 Houck, J. C., & Bregman, J. N. 1990, ApJ, 352, 506
 Jackson, J. M., Simon, R., Shah, R., Rathborne, J., Heyer, M. H., Clemens, D. P., & Bania, T. M. 2004, in Astronomical Society of the Pacific Conference Series, Vol. 317, Milky Way Surveys: The Structure and Evolution of our Galaxy, ed. D. Clemens, R. Shah, & T. Brainerd, 49
 Kalberla, P. M. W., Burton, W. B., Hartmann, D., Arnal, E. M., Bajaja, E., Morras, R., & Pöppel, W. G. L. 2005, A&A, 440, 775
 Kalberla, P. M. W., Dedes, L., Kerp, J., & Haud, U. 2007, A&A, 469, 511
 Kerr, F. J., & Lynden-Bell, D. 1986, MNRAS, 221, 1023
 Kerton, C. R., Knee, L. B. G., & Schaeffer, A. J. 2006, AJ, 131, 1501
 Koo, B.-C., Heiles, C., & Reach, W. T. 1992, ApJ, 390, 108
 Koo, B.-C., & McKee, C. F. 1992, ApJ, 388, 93
 Lockman, F. J. 1981, ApJ, 245, 459
 —. 1984, ApJ, 283, 90
 —. 2002, ApJ, 580, L47
 Luna, A., Bronfman, L., Carrasco, L., & May, J. 2006, ApJ, 641, 938
 Mac Low, M.-M., McCray, R., & Norman, M. L. 1989, ApJ, 337, 141
 McClure-Griffiths, N. M., & Dickey, J. M. 2007, ApJ, 671, 427
 McClure-Griffiths, N. M., Dickey, J. M., Gaensler, B. M., & Green, A. J. 2002, ApJ, 578, 176
 McClure-Griffiths, N. M., Dickey, J. M., Gaensler, B. M., Green, A. J., Haverkorn, M., & Strasser, S. 2005, ApJS, 158, 178
 McClure-Griffiths, N. M., Ford, A., Pisano, D. J., Gibson, B. K., Staveley-Smith, L., Calabretta, M. R., Dedes, L., & Kalberla, P. M. W. 2006, ApJ, 638, 196
 Morras, R., Bajaja, E., Arnal, E. M., & Pöppel, W. G. L. 2000, A&AS, 142, 25
 Nagashima, M., Inutsuka, S.-i., & Koyama, H. 2006, ApJ, 652, L41
 Norman, C. A., & Ikeuchi, S. 1989, ApJ, 345, 372
 Paladini, R., Davies, R. D., & DeZotti, G. 2004, MNRAS, 347, 237
 Press, W. H., Teukolsky, S. A., Vetterling, W. T., & Flannery, B. P. 1992, Numerical recipes in C. The art of scientific computing (Cambridge: University Press, —c1992, 2nd ed.)
 Putman, M. E., Bland-Hawthorn, J., Veilleux, S., Gibson, B. K., Freeman, K. C., & Maloney, P. R. 2003, ApJ, 597, 948
 Putman, M. E. et al. 2002, AJ, 123, 873
 Richter, P., Savage, B. D., Wakker, B. P., Sembach, K. R., & Kalberla, P. M. W. 2001a, ApJ, 549, 281
 Richter, P., Sembach, K. R., Wakker, B. P., Savage, B. D., Tripp, T. M., Murphy, E. M., Kalberla, P. M. W., & Jenkins, E. B. 2001b, ApJ, 559, 318
 Rougoor, G. W., & Oort, J. H. 1960, Proceedings of the National Academy of Science, 46, 1
 Sato, M. et al. 2007, PASJ, 59, 743

Shapiro, P. R., & Field, G. B. 1976, ApJ, 205, 762
 Stanimirović, S. et al. 2006, ApJ, 653, 1210
 Staveley-Smith, L. et al. 1996, Publications of the Astronomical Society of Australia, 13, 243
 Stil, J. M. et al. 2006, ApJ, 637, 366
 Tomisaka, K., & Ikeuchi, S. 1988, ApJ, 330, 695
 Vallée, J. P. 2008, AJ, 135, 1301
 van Woerden, H., Rougoor, W., & Oort, J. 1957, Comptes rendus de l'Académie des sciences, 244, 1691
 Wakker, B. P. 1991, A&A, 250, 499
 Wakker, B. P., & van Woerden, H. 1991, A&A, 250, 509

Wakker, B. P., York, D. G., Wilhelm, R., Barentine, J. C., Richter, P., Beers, T. C., Ivezić, Ž., & Howk, J. C. 2008, ApJ, 672, 298
 Weiner, B. J., Vogel, S. N., & Williams, T. B. 2001, in Astronomical Society of the Pacific Conference Series, Vol. 240, Gas and Galaxy Evolution, ed. J. E. Hibbard, M. Rupen, & J. H. van Gorkom, 515
 Williams, D. R. W. 1973, A&AS, 8, 505

TABLE 1
 HI CLOUDS - OBSERVED PROPERTIES

l (deg)	b (deg)	V_{LSR} (km s ⁻¹)	T_{pk}^{a} (K)	Δv (km s ⁻¹)	N_{HI} ($\times 10^{19}$ cm ⁻²)	$\theta_{\text{min}} \times \theta_{\text{maj}}^{\text{b}}$ ($' \times '$)	$M_{\text{HI}} d^{-2}$ ^c (M_{\odot} kpc ⁻²)	Notes
324.78	13.39	-91.1 ± 4.2	0.20	8.8 ± 3.3	0.34 ± 0.18	24 × 38	6.3	
324.87	-8.30	-73.2 ± 2.2	1.16	12.7 ± 1.1	2.87 ± 0.31	17 × 36	18.6	
325.11	-8.56	-80.5 ± 6.3	0.34	18.2 ± 3.9	1.20 ± 0.37	28 × 36	24.0	
325.34	-4.61	-94.2 ± 1.8	0.44	6.1 ± 1.3	0.52 ± 0.14	27 × 29	20.5	
325.38	5.14	-88.4 ± 2.2	0.78	10.3 ± 1.2	1.56 ± 0.24	26 × 40	29.3	

NOTE. — Observed properties of H I clouds in the GASS pilot region. The complete version of Table 1 is available in the electronic edition of the Astrophysical Journal. We provide this sample as a guide to its content. Descriptions of each property are presented in §3.2. Clouds that have been cataloged elsewhere in the literature are noted by the following labels:

1: detected by Putman et al. (2002) and

2: detected by Wakker & van Woerden (1991).

Although the clouds detected elsewhere do not necessarily have the exact Galactic coordinates and V_{LSR} as listed here, it is likely that they are the same cloud and that the differences are a result of observational constraints. Also, we note that Morras et al. (2000) detected H I in some areas of these clouds but such detections were not identified as individual objects.

^a Uncertainties in T_{pk} are 0.07 K.

^b Uncertainties in the maximum angular extents are dominated by background levels surrounding the cloud and are assumed to be 25% of the estimated values.

^c Mass uncertainties are dominated by the interactive process used in mass determination and are assumed to be 40% of the estimated values.

TABLE 2
 TANGENT POINT H I CLOUDS - DERIVED PROPERTIES

l (deg)	b (deg)	V_{LSR} (km s ⁻¹)	V_{dev} (km s ⁻¹)	d (kpc)	R^{a} (kpc)	z (kpc)	r (pc)	M_{HI} (M_{\odot})
325.34	-4.61	-94.2 ± 1.8	-1.7 ± 3.5	7.0 ± 1.5	4.8 ^{+0.4}	-0.56 ± 0.12	29 ± 8	1000 ± 600
325.69	-2.87	-98.8 ± 0.7	-3.9 ± 3.1	7.0 ± 1.5	4.8 ^{+0.4}	-0.35 ± 0.07	25 ± 7	470 ± 270
325.95	-3.33	-103.2 ± 0.9	-6.1 ± 3.1	7.0 ± 1.4	4.8 ^{+0.4}	-0.41 ± 0.08	34 ± 9	700 ± 400
326.34	-4.47	-118.0 ± 3.6	-19.7 ± 4.7	7.1 ± 1.3	4.7 ^{+0.3}	-0.55 ± 0.10	27 ± 7	270 ± 140
327.65	13.25	-108.3 ± 6.6	-4.5 ± 7.3	7.4 ± 1.9	4.5 ^{+0.6}	1.69 ± 0.44	38 ± 12	600 ± 400
328.24	2.67	-135.0 ± 2.5	-24.7 ± 3.9	7.2 ± 1.4	4.5 ^{+0.4}	0.34 ± 0.06	24 ± 6	1200 ± 700
329.79	3.74	-112.0 ± 1.5	-0.8 ± 3.4	7.4 ± 1.9	4.3 ^{+0.6}	0.48 ± 0.12	30 ± 9	1800 ± 1200
330.12	-3.40	-129.3 ± 2.0	-18.8 ± 3.6	7.4 ± 0.8	4.2 ^{+0.2}	-0.44 ± 0.05	30 ± 6	120 ± 50
330.79	4.34	-114.1 ± 1.9	-5.5 ± 3.6	7.4 ± 0.9	4.2 ^{+0.3}	0.56 ± 0.07	24 ± 5	1100 ± 500
330.85	13.32	-138.3 ± 10.1	-31.6 ± 10.6	7.6 ± 0.6	4.1 ^{+0.1}	1.76 ± 0.14	36 ± 7	240 ± 100
330.90	6.35	-120.3 ± 7.8	-11.1 ± 8.4	7.5 ± 0.9	4.1 ^{+0.2}	0.83 ± 0.10	25 ± 5	440 ± 200
330.91	5.74	-115.0 ± 4.5	-5.7 ± 5.4	7.5 ± 0.9	4.1 ^{+0.3}	0.75 ± 0.09	30 ± 7	110 ± 50
331.04	12.43	-114.6 ± 6.3	-6.5 ± 7.0	7.6 ± 0.9	4.1 ^{+0.3}	1.64 ± 0.20	48 ± 10	1000 ± 500
331.06	3.87	-119.7 ± 2.1	-9.2 ± 3.6	7.5 ± 0.9	4.1 ^{+0.3}	0.50 ± 0.06	27 ± 6	2400 ± 1100
331.20	10.53	-109.0 ± 4.5	-1.3 ± 5.4	7.6 ± 1.0	4.1 ^{+0.3}	1.38 ± 0.18	26 ± 6	280 ± 140
331.25	-5.41	-113.2 ± 3.3	-4.5 ± 4.4	7.5 ± 1.0	4.1 ^{+0.3}	-0.71 ± 0.09	48 ± 10	5700 ± 2700
331.33	-3.40	-135.5 ± 3.0	-26.8 ± 4.2	7.5 ± 0.7	4.1 ^{+0.2}	-0.44 ± 0.04	46 ± 9	300 ± 130
331.46	3.40	-112.4 ± 3.6	-3.4 ± 4.7	7.5 ± 1.0	4.1 ^{+0.3}	0.44 ± 0.06	41 ± 9	4900 ± 2300
332.64	8.16	-115.0 ± 2.4	-4.9 ± 3.9	7.6 ± 1.1	3.9 ^{+0.3}	1.08 ± 0.15	28 ± 6	120 ± 60
332.66	-5.34	-115.7 ± 1.1	-4.6 ± 3.2	7.6 ± 1.1	3.9 ^{+0.3}	-0.71 ± 0.10	31 ± 7	2000 ± 1000
332.73	-3.47	-112.7 ± 2.0	-0.7 ± 3.6	7.6 ± 1.1	3.9 ^{+0.3}	-0.46 ± 0.06	20 ± 5	800 ± 400
332.79	-6.41	-132.2 ± 5.5	-20.4 ± 6.2	7.6 ± 0.8	3.9 ^{+0.2}	-0.85 ± 0.09	33 ± 7	800 ± 400
332.86	-2.73	-143.7 ± 2.7	-29.7 ± 4.0	7.6 ± 0.8	3.9 ^{+0.2}	-0.36 ± 0.04	25 ± 5	340 ± 150
332.87	-2.07	-151.4 ± 5.7	-37.4 ± 6.4	7.6 ± 0.8	3.9 ^{+0.2}	-0.27 ± 0.03	24 ± 5	230 ± 100
333.18	-9.24	-114.4 ± 1.5	-1.0 ± 3.4	7.7 ± 1.1	3.8 ^{+0.3}	-1.23 ± 0.17	37 ± 8	460 ± 220
333.19	-5.61	-128.8 ± 2.9	-14.6 ± 4.2	7.6 ± 1.0	3.8 ^{+0.2}	-0.75 ± 0.10	33 ± 7	900 ± 400
333.20	-3.87	-116.2 ± 2.7	-1.7 ± 4.1	7.6 ± 1.1	3.8 ^{+0.3}	-0.51 ± 0.07	30 ± 7	900 ± 400
333.26	-5.21	-115.4 ± 1.2	-1.0 ± 3.2	7.6 ± 1.1	3.8 ^{+0.3}	-0.69 ± 0.10	46 ± 10	5100 ± 2500
333.51	-9.44	-133.4 ± 8.0	-21.4 ± 8.5	7.7 ± 0.8	3.8 ^{+0.2}	-1.27 ± 0.13	29 ± 6	340 ± 150

TABLE 2 — *Continued*

l (deg)	b (deg)	V_{LSR} (km s ⁻¹)	V_{dev} (km s ⁻¹)	d (kpc)	R^a (kpc)	z (kpc)	r (pc)	M_{HI} (M_{\odot})
333.53	-2.67	-126.2 ± 6.1	-12.5 ± 6.8	7.6 ± 1.0	3.8 ^{+0.2}	-0.35 ± 0.05	20 ± 4	270 ± 130
333.53	3.27	-130.4 ± 0.8	-16.8 ± 3.1	7.6 ± 0.9	3.8 ^{+0.2}	0.43 ± 0.05	33 ± 7	550 ± 260
333.67	-3.20	-122.6 ± 4.3	-7.4 ± 5.3	7.6 ± 1.0	3.8 ^{+0.3}	-0.43 ± 0.06	23 ± 5	550 ± 270
333.80	-4.67	-132.5 ± 1.7	-16.0 ± 3.4	7.7 ± 0.9	3.8 ^{+0.2}	-0.62 ± 0.07	19 ± 4	280 ± 130
334.13	-2.60	-124.8 ± 1.8	-8.2 ± 3.5	7.7 ± 1.0	3.7 ^{+0.3}	-0.35 ± 0.05	23 ± 5	230 ± 110
334.33	3.80	-124.4 ± 2.2	-5.2 ± 3.7	7.7 ± 1.0	3.7 ^{+0.3}	0.51 ± 0.07	29 ± 6	400 ± 190
334.46	-4.47	-123.0 ± 2.3	-1.7 ± 3.8	7.7 ± 1.1	3.7 ^{+0.3}	-0.60 ± 0.08	38 ± 9	2000 ± 1000
334.47	3.00	-127.3 ± 1.8	-5.8 ± 3.5	7.7 ± 1.0	3.7 ^{+0.3}	0.40 ± 0.05	31 ± 7	900 ± 400
334.60	-3.00	-134.3 ± 4.4	-12.5 ± 5.3	7.7 ± 1.0	3.6 ^{+0.2}	-0.40 ± 0.05	26 ± 6	570 ± 270
334.80	-7.82	-136.3 ± 2.2	-15.0 ± 3.7	7.8 ± 1.0	3.6 ^{+0.2}	-1.06 ± 0.14	42 ± 9	560 ± 270
334.93	-11.95	-131.5 ± 8.0	-12.0 ± 8.6	7.9 ± 1.0	3.6 ^{+0.2}	-1.63 ± 0.21	35 ± 8	570 ± 270
335.00	0.80	-136.5 ± 1.9	-14.4 ± 3.5	7.7 ± 1.0	3.6 ^{+0.2}	0.11 ± 0.01	28 ± 6	220 ± 100
335.01	-7.22	-123.6 ± 2.2	-2.5 ± 3.7	7.8 ± 1.1	3.6 ^{+0.3}	-0.98 ± 0.14	30 ± 7	220 ± 110
335.07	-6.62	-128.2 ± 1.5	-7.0 ± 3.3	7.8 ± 1.1	3.6 ^{+0.3}	-0.89 ± 0.12	25 ± 6	200 ± 90
335.07	-4.88	-123.4 ± 2.8	-1.9 ± 4.1	7.7 ± 1.1	3.6 ^{+0.3}	-0.66 ± 0.09	31 ± 7	610 ± 300
335.13	-4.40	-142.7 ± 4.8	-20.7 ± 5.7	7.7 ± 0.8	3.6 ^{+0.2}	-0.59 ± 0.06	38 ± 8	800 ± 400
335.13	3.00	-139.4 ± 2.3	-17.2 ± 3.8	7.7 ± 0.9	3.6 ^{+0.2}	0.40 ± 0.05	39 ± 8	900 ± 400
335.20	-5.88	-124.5 ± 3.0	-1.9 ± 4.2	7.8 ± 1.1	3.6 ^{+0.3}	-0.79 ± 0.11	24 ± 5	180 ± 90
335.20	4.54	-133.5 ± 2.6	-10.7 ± 4.0	7.7 ± 1.0	3.6 ^{+0.3}	0.61 ± 0.08	28 ± 6	350 ± 170
335.27	-2.47	-126.6 ± 2.2	-2.2 ± 3.7	7.7 ± 1.1	3.6 ^{+0.3}	-0.33 ± 0.05	32 ± 7	3200 ± 1600
335.27	2.13	-127.0 ± 2.0	-2.5 ± 3.6	7.7 ± 1.1	3.6 ^{+0.3}	0.29 ± 0.04	25 ± 6	600 ± 300
335.33	4.07	-128.8 ± 1.5	-4.3 ± 3.4	7.7 ± 1.1	3.5 ^{+0.3}	0.55 ± 0.08	53 ± 12	2300 ± 1100
335.74	-5.07	-151.0 ± 1.6	-22.4 ± 3.4	7.8 ± 0.8	3.5 ^{+0.2}	-0.69 ± 0.07	58 ± 12	3200 ± 1400
335.94	-4.07	-141.2 ± 2.3	-11.5 ± 3.8	7.8 ± 1.0	3.5 ^{+0.2}	-0.55 ± 0.07	32 ± 7	1100 ± 500
336.00	2.40	-132.6 ± 0.8	-3.5 ± 3.1	7.8 ± 1.1	3.5 ^{+0.3}	0.33 ± 0.05	17 ± 4	70 ± 30
336.20	3.13	-129.8 ± 1.0	-0.2 ± 3.2	7.8 ± 1.1	3.4 ^{+0.3}	0.43 ± 0.06	27 ± 6	1200 ± 600
336.87	-5.01	-141.3 ± 5.0	-13.2 ± 5.8	7.8 ± 1.0	3.3 ^{+0.2}	-0.68 ± 0.09	49 ± 11	5100 ± 2400
336.94	6.08	-139.6 ± 4.1	-12.3 ± 5.1	7.9 ± 1.0	3.3 ^{+0.2}	0.83 ± 0.11	30 ± 7	490 ± 240
337.01	-5.14	-132.3 ± 3.2	-4.7 ± 4.4	7.9 ± 1.1	3.3 ^{+0.3}	-0.70 ± 0.10	44 ± 10	4000 ± 1900
337.27	-2.94	-127.5 ± 2.1	-0.3 ± 3.7	7.8 ± 1.1	3.3 ^{+0.3}	-0.40 ± 0.06	41 ± 9	12000 ± 6000
337.35	-4.47	-145.0 ± 1.3	-18.9 ± 3.3	7.9 ± 0.9	3.3 ^{+0.2}	-0.61 ± 0.07	26 ± 5	100 ± 50
337.55	5.41	-146.4 ± 3.3	-20.6 ± 4.5	7.9 ± 0.8	3.2 ^{+0.2}	0.74 ± 0.08	39 ± 8	190 ± 90
337.61	16.01	-131.1 ± 18.9	-8.6 ± 19.1	8.2 ± 1.1	3.2 ^{+0.3}	2.25 ± 0.30	32 ± 7	170 ± 80
337.87	-2.47	-145.4 ± 1.8	-16.6 ± 3.5	7.9 ± 0.9	3.2 ^{+0.3}	-0.34 ± 0.04	44 ± 9	3600 ± 1700
337.87	2.60	-137.4 ± 1.2	-8.6 ± 3.2	7.9 ± 1.0	3.2 ^{+0.3}	0.36 ± 0.05	29 ± 6	230 ± 110
337.88	-5.07	-155.1 ± 5.4	-26.6 ± 6.2	7.9 ± 0.8	3.2 ^{+0.2}	-0.70 ± 0.07	52 ± 11	1100 ± 500
337.88	-3.80	-152.2 ± 2.0	-23.5 ± 3.6	7.9 ± 0.8	3.2 ^{+0.2}	-0.52 ± 0.05	31 ± 6	380 ± 170
337.94	-3.13	-142.5 ± 2.0	-13.9 ± 3.6	7.9 ± 1.0	3.2 ^{+0.3}	-0.43 ± 0.05	30 ± 6	1100 ± 500
337.94	4.14	-147.4 ± 4.5	-18.9 ± 5.4	7.9 ± 0.9	3.2 ^{+0.3}	0.57 ± 0.07	40 ± 8	600 ± 280
337.99	17.47	-176.0 ± 4.1	-53.4 ± 5.1	8.3 ± 0.4	3.2 ^{+0.1}	2.48 ± 0.11	34 ± 6	240 ± 100
338.40	-2.33	-152.8 ± 2.7	-25.1 ± 4.0	7.9 ± 0.8	3.1 ^{+0.2}	-0.32 ± 0.03	33 ± 7	800 ± 400
338.54	-3.74	-159.8 ± 4.1	-30.0 ± 5.1	7.9 ± 0.7	3.1 ^{+0.1}	-0.52 ± 0.04	43 ± 8	550 ± 240
339.08	-3.13	-134.2 ± 1.9	-0.4 ± 3.6	8.0 ± 1.1	3.0 ^{+0.3}	-0.43 ± 0.06	37 ± 8	2700 ± 1300
339.29	-5.07	-141.4 ± 2.3	-5.5 ± 3.8	8.0 ± 1.0	3.0 ^{+0.3}	-0.71 ± 0.09	40 ± 9	1000 ± 500
339.65	8.36	-140.0 ± 4.9	-6.3 ± 5.8	8.1 ± 1.1	3.0 ^{+0.3}	1.17 ± 0.15	50 ± 11	800 ± 400
339.88	2.13	-153.9 ± 5.0	-18.1 ± 10.3	8.0 ± 0.9	2.9 ^{+0.2}	0.30 ± 0.03	31 ± 7	900 ± 400
340.25	-5.94	-144.6 ± 5.4	-9.5 ± 10.5	8.0 ± 1.0	2.9 ^{+0.3}	-0.83 ± 0.10	30 ± 6	1000 ± 500
340.35	-2.87	-142.3 ± 2.5	-7.6 ± 9.3	8.0 ± 1.0	2.9 ^{+0.3}	-0.40 ± 0.05	43 ± 9	2100 ± 1000
340.41	2.40	-164.8 ± 3.0	-29.5 ± 9.5	8.0 ± 0.8	2.9 ^{+0.2}	0.34 ± 0.03	35 ± 7	1300 ± 600
341.65	-4.47	-150.5 ± 4.9	-6.8 ± 10.2	8.1 ± 1.0	2.7 ^{+0.3}	-0.63 ± 0.08	33 ± 7	370 ± 170
342.68	16.98	-177.4 ± 12.4	-35.7 ± 15.3	8.5 ± 0.6	2.5 ^{+0.1}	2.48 ± 0.17	27 ± 5	200 ± 80
342.91	3.54	-149.2 ± 3.9	0.4 ± 9.8	8.1 ± 0.8	2.5 ^{+0.2}	0.50 ± 0.05	31 ± 6	340 ± 150

NOTE. — Derived properties of a subset of the clouds assumed to be located at tangent points (those with $V_{\text{dev}} \leq 0.8$ km s⁻¹).

^a Along a given line-of-sight, the smallest Galactocentric radius possible is at the tangent point. If the cloud is not located at the tangent point it must be further away from the center and the error on R must be positive.

TABLE 3
PROPERTY SUMMARY AND COMPARISON TO LOCKMAN CLOUDS

Parameter	This Sample		Lockman (2002)	
	Median	90% Range	Median	90% Range
T_{pk} (K)	0.6	0.2 → 2.2	1.0	0.4 → 2.7
Δv (km s ⁻¹)	12.8	5.8 → 26.2	12.2	5.4 → 26.3
N_{HI} ($\times 10^{19}$ cm ⁻²)	1.4	0.2 → 2.2	2	0.7 → 6.3
r (pc)	32	< 23 → 50	12	< 9.5 → 17.5
M_{HI} (M_{\odot})	630	120 → 4850	50	12 → 290

TABLE 3 — *Continued*

Parameter	This Sample		Lockman (2002)	
	Median	90% Range	Median	90% Range
$ z $ (pc)	560	320 → 1690	940	640 → 1210
σ_{cc} (km s ⁻¹)	16 – 22		15 – 20	

NOTE. — Median values of the observed halo cloud properties in this sample, where the number of clouds $n = 403$ for T_{pk} , Δv , and N_{HI} and $n = 81$ for remaining properties (of tangent point clouds) and the Lockman (2002) sample, where $n = 38$. Most properties have a large scatter about the median in both samples, as demonstrated by the 90% range.